Title： A biofidelic Goat Model of Traumatic Optic Neuropathy with Optic Canal Fracture via Transnasal Endoscopy

Running title: Large Animal Model of traumatic optic neuropathy

Zhonghao Yu[1,2#]; Hengzhuo Duan[4#] ; Tonghe Yang[1,2#]; Yi Cao[1,2]; Shudong Tian[1,2]; Huan Wu[1,2]; Jiale Zhang[1,2]; Yue Wang[1,2]; Ruixin Zhou[1,2]; Shengjian Lu[1,2]; Boyue Xu[1,2]; Mengyun Li[6]; Tian Xia[1,5]; Si Zhang[7]; Haodi Chen[1,2]; Shurui Huang[1,2]; Yikui Zhang[1,2*]; Jian Yang[4,1*]; Wencan Wu[1,2,3*]

[1] State Key Laboratory of Ophthalmology, Optometry and Vision Science, Eye Hospital, Wenzhou Medical University, Wenzhou, China

[2] Zhejiang Key Laboratory of Key Technologies for Visual Pathway Reconstruction, Eye Hospital, Wenzhou Medical University, Wenzhou, China

[3] Oujiang Laboratory (Zhejiang Lab for Regenerative Medicine, Vision and Brain Health), Wenzhou, Zhejiang, China

[4] Beijing Engineering Research Center of Mixed Reality and Advanced Display, School of Optics and Photonics, Beijing Institute of Technology; Beijing, 100081, China

[5] Department of Ophthalmology, Jinhua Municipal Central Hospital, Jinhua Hospital of Zhejiang University; Jinhua, Zhejiang, 321000, China

[6] Medical Research Center, Shaoxing People's Hospital, Zhejiang University Shaoxing Hospital; Shaoxing, Zhejiang, 312035, China

[7] Department of Ophthalmology, The First People's Hospital of Foshan; Foshan, Guangdong, 528000, China.

# Z.Y., H.D., T.Y. contributed equally to this work.

* To whom correspondence should be addressed.

Yikui Zhang: zhang.yikui@wmu.edu.cn

Jian Yang: jyang@bit.edu.cn

Wencan Wu: wuwencan@wmu.edu.cn

Abstract

Traumatic optic neuropathy (TON) is a major cause of irreversible vision loss following blunt cranial trauma, yet the absence of clinically relevant large animal models that faithfully recapitulate human TON has significantly impeded translational research. Current rodent models do not reproduce optic canal fracture, a key injury mechanism in many patients with TON. Here, we combined high-fidelity finite element analysis (FEA) with iterative engineering to establish a reproducible goat model of TON. We first built a high-resolution human-head finite element model to characterize force transmission to the optic nerve. Across clinically relevant periorbital impacts, stress preferentially concentrated in the intracanalicular segment, reaching a peak force density of approximately 500 N/m² at 50.6 ms, about fivefold higher than in the intraorbital segment. Simulations further showed that direct optic canal impact reproduced comparable intracanalicular stress with a markedly lower input force: 195 N, compared with 3900 N for periorbital impact. Guided by these insights, we developed transnasal endoscopic impact systems capable of inducing optic canal fractures in goats. TON was confirmed within 24 hours by a characteristic relative afferent pupillary defect (RAPD), and at 1 month post-injury goats (n = 14) exhibited a 10%–20% reduction in ganglion cell complex (GCC) thickness and 40%–65% reductions in flash visual evoked potential (FVEP) and pattern electroretinogram (PERG) amplitude ratios (all $P \leq 0.001$), with structural and functional preservation of the fellow eye. This study presents a robust, standardized, and clinically relevant large-animal platform for investigating TON pathophysiology.

Keywords:

traumatic optic neuropathy; finite element analysis; large-animal model; transnasal endoscopy; optic canal

Text

Introduction

Optic neuropathies represent a leading cause of irreversible blindness worldwide, posing a significant challenge to modern ophthalmology despite advances in our understanding of central nervous system regeneration (Laha et al., 2017; Lee et al., 2024). Recent studies have identified key intrinsic and extrinsic mechanisms regulating retinal ganglion cell (RGC) survival and axon regeneration (Benowitz et al., 2017). However, translating these findings into clinical practice remains stalled (Tsai et al., 2024). A major barrier to bridging this translational gap is the absence of large-animal models. Current models fail to accurately recapitulate the anatomical, biomechanical, and pathological features of human optic neuropathy (Zhang et al., 2021). Moreover, most existing experimental paradigms are defined empirically rather than by quantitatively grounded cranio-orbital biomechanics, limiting standardization and cross-study comparability.

TON serves as a particularly valuable disease paradigm within the spectrum of optic neuropathies (Chen et al., 2022). Characterized by an acute onset and a well-defined injury site (Yu-Wai-Man, 2015), TON shares pathological features with glaucoma but offers a more precise temporal window for therapeutic intervention. Currently, TON research has relied heavily on rodent models. However, the rodent visual system differs fundamentally from that of humans. Specifically, rodents lack a true collagenous lamina cribrosa and possess a vastly different optic canal and craniofacial skeletal architecture (Ibrahim et al., 2018; Tao et al., 2017). Furthermore, commonly used ultrasound-based or optic nerve crush models often lack the biomechanical fidelity of clinical optic canal fractures and induce widespread collateral damage to periorbital tissues (Tang et al., 2011; Tao et al., 2017). Together, these limitations highlight the need for a clinically grounded large-animal model that captures optic canal–related injury mechanics in a standardized and quantitative manner.

To address these limitations, we sought to establish a model in a species with closer anatomical similarity to humans. Our previous comparative anatomical studies identified the goat *(Capra hircus)* as an optimal candidate (Zhang et al., 2022). Unlike rodents, goats possess an optic canal and sphenoid sinus structure highly similar to human anatomy, making them amenable to transnasal endoscopic access. In this study, we first employed finite element analysis (FEA) to map stress distributions under periorbital trauma and identified localized optic canal impact as an efficient modeling strategy. Based on these findings, we engineered a standardized impact system and applied it transnasally under endoscopic guidance to induce an optic canal fracture, thereby establishing a highly reproducible goat model of TON that closely recapitulates the clinical features of the human condition.

Materials and methods

All materials used in the study are listed in Table S1.

Animals

Male Saanen goats (4–7 months old) were purchased from Caimu Livestock Company (Hangzhou, China) and housed at the Wenzhou Medical University animal facility. This age was chosen to provide adequate cranio-orbital development for endoscopic surgery while keeping the animals a manageable size for standardized positioning. All experimental animals were housed in temperature-controlled rooms under a regular light–dark cycle, with unrestricted access to food and water. Animals were allowed a minimum acclimatization period of one week prior to the initiation of experiments. Importantly, perioperative mortality directly related to the surgical impact procedures and anesthesia was 0%. Approximately 10% of animals experienced mild, transient rhinorrhea during the first 1–2 days postoperatively. All affected animals were treated with a 5-day course of antibiotics (gentamicin plus ceftiofur), and symptoms fully resolved. In addition, animals were excluded from analysis if they failed

to meet the functional inclusion criterion within 24 hours post-injury (PLR grade difference ≥ 2). All experiments were approved by the Institutional Animal Care and Use Committee at Wenzhou Medical University (Wenzhou, China, ID number: wydw2022-0523). A total of 18 male Saanen goats were successfully included and analyzed. The animals were allocated into three experimental cohorts: the gas-driven impactor group (n=8), the elastic-energy impactor group (n=6), and a dedicated pathology group for histological validation (n=4). In all animals, the left eye underwent optic canal impact, while the contralateral right eye served as an internal control.

Finite element analysis

Finite element simulations were performed using COMSOL Multiphysics 6.0 to quantify the transient stress response of the optic nerve under head-impact loading. The workflow comprised CT-based geometry reconstruction, tetrahedral meshing, boundary condition settings, and time-dependent dynamic analysis under prescribed impact force.

Geometry Reconstruction and Meshing

An anonymized head CT dataset (continuous slice thickness: 0.7 mm) was used to reconstruct the subject-specific geometry. The CT images were acquired using a SOMATOM go.Top CT scanner (Siemens Healthineers, Germany). The dataset was obtained with informed consent under an institutional review board–approved protocol (IRB no. 2024-065-K-57-03), in accordance with the Declaration of Helsinki. To improve computational efficiency, a simplified head model was constructed (Li et al., 2020), incorporating five key components: the optic nerve, skull, eyeball, extraocular muscles, and tendons. This model omitted complex structures such as the brain and blood vessels, including only five biological tissues: the unilateral optic nerve, skull, eyeball, extraocular muscles, and tendons. Intracranial soft tissues (e.g., brain

parenchyma) were excluded to focus computational resources on the orbital region. Image segmentation was performed in 3D Slicer (v5.0.2). The skull was extracted via HU thresholding (200~2000 HU) followed by post-processing steps including hole filling and island removal (Maire and Withers, 2014). The optic nerve, eyeball, extraocular muscles, and tendons were manually delineated based on anatomical landmarks. The segmented label maps were then converted into 3D surface meshes and processed using Laplacian smoothing (iterations = 30, λ= 0.5) to minimize staircase artifacts inherent to voxel-based reconstruction. Upon completion of geometric processing, the smoothed surface models were exported in Standard Tessellation Language (STL) format.

These STL files were then imported into COMSOL Multiphysics 6.0 for volumetric meshing and simulation. The domain was discretized using linear tetrahedral elements. The global element size range was set to 2.5~14 mm, with adaptive local refinement applied near the optic nerve to a minimum size of 0.6 mm (growth rate = 1.5). The final mesh comprised 173,215 tetrahedral elements.

Material properties

In this study, the modeling of all structures was conducted using isotropic and homogeneous material properties. The focus for elastic materials was placed on three fundamental mechanical parameters: Young's modulus (E), Poisson's ratio (ν), and density (ρ). Specifically, the skull was modeled using a linear elastic material model with a Young's modulus of 14.5 GPa and a Poisson's ratio of 0.35. Given the contrast in compressibility between tissues such as muscles and ligaments and the near incompressibility of the eyeball, the latter was modeled with a material having a Poisson's ratio close to 0.5 (Li et al., 2020) to reflect its incompressible nature. Moreover, the biomechanical behavior of the optic nerve was represented using a linear viscoelastic material model widely adopted in numerical models, assuming that the time-

varying shear modulus is independent of strain magnitude. Material parameters for head tissues were referenced from previous literature (Li et al., 2020), and a comprehensive table of material properties is provided in this document (Table 1).

For the mathematical description of linear viscoelastic materials, the generalized Maxwell model was approximated using the Prony series. The linear viscoelastic model was expressed by the following equation:

$$E(t) = E_\infty + \sum_{i=1}^{N} E_i e^{-t/\tau_i}$$

where E_∞ represents the material's stiffness at infinite time, E_i is the stiffness at the i time point, and τ_i is the corresponding relaxation time. The shear modulus $G(t)$ was calculated as:

$$G(t) = G_0(1 - \sum_{i=1}^{N} g_i) + \sum_{i=1}^{N} g_i G_0 e^{-t/\tau_i}$$

here, $g_i = G_i/G_0$, with G_0 being the instantaneous shear modulus. Through this methodology, our study accurately simulated the complex behaviors of biological tissues under load and provided a reliable numerical method for advancing the understanding of biomechanical phenomena.

Detailed settings of material property parameters are shown in Table1.

Boundary condition setting and analysis

Transient dynamic analyses were conducted using the solid mechanics module of COMSOL Multiphysics. This research was designed with reference to the simulation studies on the impact of cylindrical projectiles on the skull by Huempfner-Hierl (Huempfner-Hierl et al., 2015) and the demonstration by Chen (Chen and Ostoja-Starzewski, 2010) that the time course of the impact force during collisions approximates a Gaussian function. Impact loading was prescribed as a transient total force F(t) governed by a Gaussian function:

$$F(t) = F_{max} \cdot \exp\left(-\frac{(t-t_0)^2}{2\sigma^2}\right)$$

where F_{max}= 3900 N, t_0= 50 ms, and σ= 10 ms. To implement this load on the finite element mesh, the total force was applied as a uniformly distributed surface traction over an elliptical contact patch (Area = 1 cm^2). Mathematically, the applied boundary traction $T(t)$ was defined as the total force normalized by the contact area:

$$T(t) = \frac{F(t)}{Area}$$

Fixed constraints were applied to nodes on the skull base. To investigate the sensitivity of the optic nerve to impact location, loads were applied to four quadrants of the orbital rim (superior, inferior, lateral, medial) and directly to the optic canal region. Directional sensitivity was assessed by perturbing the loading vector by ±10° relative to the surface normal. Additionally, a parametric study was conducted by varying the skull's elastic modulus, Poisson's ratio, and density by ±10%.

All simulations were performed using the transient solver in the solid mechanics module. Time integration was executed using the Generalized-α scheme to ensure optimal control of high-frequency numerical dissipation while maintaining accuracy for inertial dynamics. A constant time step of 1.1 ms was selected for the analysis. This temporal resolution was determined based on the impact duration (t_0= 50 ms) to ensure sufficient sampling density. This resolution allowed for the accurate capture of both the Gaussian force profile and the time-dependent viscoelastic relaxation of the optic nerve, while maintaining computational efficiency. The total simulation time was set to 200 ms to observe the complete stress evolution from impact initiation to relaxation. Finally, to assess the clinical relevance of the computational results, a face validity evaluation was conducted. The simulated stress distribution patterns were qualitatively compared with typical injury locations observed in clinical cases by experienced

neuro-ophthalmologists. This qualitative comparison served to confirm that the model predicts stress concentrations in anatomically plausible regions consistent with real-world trauma.

Transnasal endoscopic procedure to expose the optic canal in goats

The procedure was described in detail in our previous study (Zhang et al., 2022) , and is further refined in the present work. General anesthesia was induced by an intravenous bolus of propofol (10 mg/kg), followed by endotracheal intubation using a 6.0-mm cuffed tube (Henan Tuoren Medical Device Co., Ltd., China). Anesthesia was maintained with 2.5–3.0% isoflurane delivered in a 1:1 mixture of oxygen and air at a flow rate of 2 L/min via a mechanical ventilator. Vital signs, including heart rate, respiratory rate, and oxygen saturation, were continuously monitored throughout the procedure using an electrocardiographic monitoring system.

To reduce intraoperative bleeding, hemocoagulase atrox was administered intravenously (1–2 U per goat) after anesthesia induction. Prophylactic antibiotics and anti-inflammatory agents were administered intravenously, including gentamicin (4 mg/kg), ceftiofur sodium (0.1 g/10 kg), and dexamethasone sodium phosphate (1 mg/kg). The corneas were protected with carbomer gel to prevent exposure-related drying.

The surgical field extended from the forehead to the nasal dorsum, with the lateral boundaries defined by the medial canthi. Hair was shaved, and the skin was disinfected three times using 5% povidone–iodine solution (Zhejiang Apeloa Inc., China). Sterile surgical drapes were applied, leaving only the nasal bridge exposed.

A midline facial incision (approximately 4–5 cm) was first made at the level of the medial canthi, followed by a vertical incision along the nasal midline (approximately 4–5 cm) and an additional inferior horizontal incision of similar length. The periosteum and underlying bone were carefully dissected using toothed forceps and a periosteal elevator. The exposed nasal bones were removed to gain access to the nasal cavity.

Upon entering the nasal cavity, an endoscopic microdebrider equipped with a straight-cut microdebrider (Medtronic, Cat. #1884004) was used to partially resect the middle turbinate and posterior olfactory mucosa on the right side, allowing exposure of the anterior bony wall of the sphenoid body. The nasal septum was then incised using a falciform knife, and partial resection of the contralateral olfactory mucosa was performed to further enlarge the operative corridor and improve visualization.

Because goats lack a naturally pneumatized sphenoid sinus anterior to the optic canal, an artificial sphenoid sinus was created. A diamond microdrill (Medtronic, Cat. #1882969) was used to thin and remove the cortical bone overlying the central anterior wall of the sphenoid body. Drilling was performed under continuous endoscopic visualization until a characteristic loss of resistance ("give-way" sensation) was encountered, indicating entry into the sphenoid cavity. Residual bone debris was removed using a blunt dissector, and hemostasis was achieved with calcium alginate packing when necessary.

The bony window of the sphenoid cavity was then gradually enlarged to obtain a clear surgical field. After removal of the packing material, the bony landmarks of the prechiasmatic region and the anterior wall of the optic canal became clearly visible. Using a combination of coarse and fine diamond burrs, the anterior bony wall of the optic canal was carefully thinned and removed until the optic canal was fully exposed, providing direct access to the intracanalicular segment of the optic nerve.

Modeling optic canal fracture in goats

The optic canal was identified at the junction of the anterior wall of the optic chiasm and the medial orbital wall under transnasal endoscopic visualization. The impactor tip was positioned in firm contact with the anterior bony wall of the optic canal, and the device was calibrated to deliver a predefined impact force. Upon activation, the metal impact rod delivered a focal

mechanical strike to the optic canal wall, resulting in a localized fracture with impinged bone that was immediately visualized endoscopically.

This impact consistently generated a circular bony fragment approximately 2 mm in diameter, which became displaced into the optic canal and produced sustained compression of the intracanalicular optic nerve. Following completion of the impact procedure, the nasal cavity was irrigated and disinfected under sterile conditions. The artificially created sphenoid sinus was packed with an absorbable gelatin sponge to achieve hemostasis, and the surgical incision was closed using 3-0 sutures. Animals were then carefully recovered from general anesthesia.

Pupillary light reflex (PLR) testing was performed prior to surgery and again 24 h post-procedure to verify successful induction of TON. Loss of PLR was consistently observed in the injured eye, while normal PLR responses were preserved in the contralateral eye.

For a detailed step-by-step guide on the surgical induction of this TON model, please refer to the Supplementary Protocol provided in the online supplementary materials.

Modified impact device and stabilizing base

To enhance the stability, reproducibility, and translational applicability of the optic canal impact model, the original high-pressure gas–driven impactor was redesigned. The conventional gas-driven system is inherently susceptible to pressure fluctuations and potential gas cylinder leakage, both of which can compromise impact consistency and experimental reproducibility. In the modified device, a motor-controlled mechanism was introduced to quantitatively stretch a compression spring, which subsequently releases stored elastic energy to propel the impact head. The spring used in this system (1.5 × 12 × 45 mm) was calibrated such that a deformation length of 20 mm produced an impact effect comparable to that of the original gas-driven device. By changing the mode of energy delivery from gas-driven to elastic

energy–driven propulsion, this elastic energy–driven impactor provided improved stability and reliability for large-animal modeling.

During optic canal fracture induction in goats, animals were positioned prone, allowing the operator to face the animal's head directly and enabling handheld use of the impact device. In contrast, nonhuman primates are typically operated in the supine position, rendering handheld impact delivery impractical and potentially unstable. To further enhance impact precision and extend the applicability of this model across species, we developed a dedicated stabilizing base for the impactor. This base incorporated five independently driven motors, which enabled multi-axis adjustment to accommodate different surgical orientations, minimize recoil, and eliminate positional deviations associated with handheld operation. Collectively, these modifications substantially improved the precision and reproducibility of optic canal fracture induction and provide a scalable platform for translational studies of TON in large-animal and nonhuman primate models.

Non-invasive visual function assessment in goats

Visual function in goats was evaluated using pupillary light reflex (PLR), optical coherence tomography (OCT), flash visual evoked potentials (FVEP), and pattern electroretinography (PERG). All procedures were performed according to standardized protocols refined from our previous work (Zhang et al., 2022), with detailed descriptions provided below.

For all examinations, endotracheal intubation was performed under laryngoscopic guidance to ensure airway patency and minimize the risk of aspiration.

For PLR, PERG, and OCT examinations, goats were sedated by intramuscular injection of xylazine (3 mg/kg). For FVEP recordings, general anesthesia was induced with intravenous propofol, followed by maintenance with inhaled isoflurane (2.5–3.0%) delivered at a flow rate of 2 L/min via endotracheal intubation.

PLR: Prior to PLR testing, animals underwent 5 min of dark adaptation to stabilize baseline pupil diameter. Eyelid specula were placed bilaterally to fully expose the globes, and artificial tears were applied to maintain corneal hydration throughout the procedure.

PLR measurements were obtained using a custom-built PLR recording system connected to a synchronized video acquisition unit and programmable light source. The camera was positioned to simultaneously capture both eyes and adjusted to achieve stable, high-resolution imaging. Recordings were performed under both visible light and infrared illumination to enable continuous, real-time monitoring of pupil dynamics.

During testing, a white-light stimulus (230 lx, 2 s duration) was delivered monocularly to elicit pupillary constriction, followed by a 12 s interval to allow full redilation. This stimulation sequence was repeated three times for each eye. The non-stimulated eye was occluded during testing to prevent consensual responses from confounding measurements.

PLR responses were graded semi-quantitatively based on pupillary reactivity: Grade 0 indicated complete absence of response; Grade 1 indicated a reduced response characterized by delayed constriction and decreased amplitude; Grade 2 indicated a brisk and robust constriction response.

OCT: For OCT imaging, topical anesthesia was achieved by instillation of proparacaine hydrochloride eye drops, followed by pharmacological mydriasis using tropicamide. Eyelid specula were applied to maintain full exposure of the pupil.

Retinal imaging was performed using a Heidelberg Spectralis OCT system (Heidelberg Engineering, Germany). The optic nerve head region was centered along the optical axis of the instrument, and peripapillary scans were acquired using a circular scanning protocol. For each eye, 100 consecutive high-resolution scans were obtained from the same retinal location and averaged using the system's built-in software to generate final images with enhanced signal-to-noise ratio. GCC thickness was quantified for subsequent analysis.

PERG: Prior to PERG recording, topical proparacaine hydrochloride and tropicamide eye drops were administered, and eyelid specula were placed bilaterally. The frontal hair was shaved, and the skin was disinfected three times using alternating povidone–iodine and 75% ethanol.

A small midline incision was made in the frontal skin, and a sterilized screw electrode was inserted into the frontal bone to serve as the ground electrode. The screw was secured using an alligator clip to ensure signal stability. Needle electrodes were placed approximately 1 cm lateral to each outer canthus as reference electrodes. ERG-Jet corneal electrodes, pre-coated with carbomer gel, were gently positioned on the center of each cornea as recording electrodes. Electrode impedance was verified to be below 10 kΩ prior to data acquisition. PERG signals were recorded using a commercial electrophysiology system (GT-2008V-III, GOTEC Co., Ltd., China). Visual stimuli were presented on two 22-inch monitors (1920 × 1080 resolution) positioned approximately 50 cm in front of each eye. The stimulus consisted of contrast-reversing black-and-white checkerboard patterns with a temporal frequency of 2.4 Hz, contrast of 96%, and mean luminance of 200 cd/m². Recordings were performed at spatial frequencies of 0.1, 0.3, 3.0, and 12.6 cycles per degree (cpd).

Signals were amplified 16,000-fold, band-pass filtered between 1 and 100 Hz, and averaged over 64 consecutive sweeps. In the averaged waveform, the first positive peak was designated as P1 (typically ~25 ms), and the first negative peak as N1 (typically ~55 ms). PERG amplitude was measured from N1 to P1. Functional outcomes were expressed as the amplitude ratio between the injured eye and the contralateral eye, with greater reductions indicating more severe RGC dysfunction.

FVEP: FVEP recordings were performed under general anesthesia using procedures identical to those described for PERG with respect to intubation, ocular preparation, hair removal, and skin disinfection. Sterilized screw electrodes were implanted in the central frontal bone and

central occipital bone to serve as reference and recording electrodes, respectively. A needle electrode placed subcutaneously near the reference electrode served as the ground. Electrode impedances were confirmed to be below 10 kΩ before recording.

Animals underwent 5 min of dark adaptation prior to testing. The tested eye was held open using an eyelid speculum, and flash stimuli of three intensities (0.025, 0.25, and 3.0 cd·s/m²) were delivered under scotopic conditions. Each stimulus intensity was recorded twice, and the averaged waveform was used for analysis. A 2 min dark adaptation interval was provided between stimulus conditions, during which artificial tears were applied to maintain corneal hydration.

Both eyes were tested separately, and the non-tested eye was occluded throughout the procedure to prevent binocular interference.

Definition of TON and severity assessment

The diagnosis of TON was based on clinical functional criteria indicative of afferent visual pathway dysfunction in the injured eye. Specifically, TON was defined by the presence of a relative afferent pupillary defect (RAPD), operationally identified as an inter-eye difference in pupillary light reflex (PLR) grade of ⩾2 within 24 h after impact (injured eye PLR grade = 0, while the contralateral eye maintained a grade of 2). Goats that did not meet this predefined criterion were excluded from subsequent analyses.

The extent and severity of TON were subsequently evaluated using continuous structural and functional outcome measures, including: (i) the percentage reduction in retinal GCC thickness of the injured eye at 1 month post-injury (1 mpi) relative to both baseline values and the contralateral eye; (ii) the percentage decrease in flash visual evoked potential (FVEP) P1–N1 amplitude ratio (injured eye/contralateral eye) relative to baseline; and (iii) the percentage decrease in pattern electroretinography (PERG) P1–N1 amplitude ratio (injured

eye/contralateral eye) relative to baseline. These quantitative indices were used for statistical analyses to compare differences across experimental groups and time points, with greater percentage reductions indicating more severe TON.

Histological Processing and Image Quantification

At one month post-injury (1 mpi), goats were euthanized, and the injured eye along with the contralateral uninjured eye (control) and their associated optic nerves were harvested. For retinal RGC quantification, each eye was cut into a cloverleaf shape, and central retinal punches were collected from each quadrant using a corneal trephine. The mean RGC count from the four retinal punches was used as the representative value for each eye. Retinal punches were fixed in 4% paraformaldehyde (PFA). To quantify RGC survival, retinal sections were immunolabeled with anti-RBPMS primary antibody (1:400, Proteintech) and appropriate fluorescent secondary antibodies, followed by imaging with a confocal microscope (20× objective). RGC in each section were manually counted using ImageJ (NIH) by a researcher blinded to experimental groups.

For optic nerve analysis, the intracanalicular segment corresponding to the primary injury site (Inj) was harvested and fixed in EM fixative containing 2% PFA and 2% glutaraldehyde. To assess axonal structural degeneration, segments were post-fixed in 1% osmium tetroxide, embedded in epoxy resin, sectioned at 1 μm, and stained with 1% para-phenylenediamine (PPD). For each nerve, five high-power fields were selected under a 100× oil immersion objective, and surviving axons were quantitatively analyzed.

Given that the contralateral uninjured eye was used as an internal control for each animal to minimize baseline variability, all quantitative comparisons between groups were performed using paired t-tests in GraphPad Prism (v9.0). Data are presented as mean ± standard deviation (SD), with statistical significance defined as $P < 0.05$.

Statistical analysis

All data are presented as mean ± SD. Normality and homogeneity of variance were assessed using the Shapiro–Wilk and Levene tests, respectively. Depending on whether these assumptions were met, data were analyzed using ordinary one-way ANOVA, two-way ANOVA, or the Scheirer–Ray–Hare non-parametric two-factor test, as specified in the figure legends. Post hoc comparisons were performed using Tukey's test or appropriate non-parametric multiple comparison procedures. A P value < 0.05 was considered statistically significant.

Results

Finite element analysis identifies the intracanalicular segment as the primary site of stress concentration

TON is a major cause of sudden and severe visual loss following blunt head trauma (Crompton, 1970; Gise et al., 2018), and the optic canal has long been implicated as the principal site of injury due to force transmission along the orbital wall (Fig. 1A)(Li et al., 2020; Wu et al., 2015). Consistent with this concept, optic canal fractures were observed in approximately 70% of TON patients in our previous multicenter clinical study (Wu et al., 2015).

We established a comprehensive three-part experimental workflow—encompassing biomechanical simulation, in vivo TON induction, and biological validation—to systematically investigate traumatic optic neuropathy (Fig. 1B). As the first step to elucidate the biomechanics of force transmission along the optic nerve, we constructed a high-fidelity finite element model based on high-resolution human skull CT scans (Fig. 1C). We simulated a clinically relevant temporal orbital wall impact using a force of 3900 N with a Gaussian distribution (Fig. 2A). Force distribution demonstrated that impact-induced forces propagated along the orbital wall and converged toward the optic canal region (Fig. 2B).

For quantitative analysis, the optic nerve was anatomically subdivided into intraorbital, intracanalicular, and intracranial segments (Fig. 2C). Following temporal periorbital impact, mechanical stress along the optic nerve central axis was preferentially concentrated within the intracanalicular segment (Fig. 2 D–F). Specifically, peak force density in the intracanalicular segment reached approximately 500 N/m² at 50.6 ms, which was nearly fivefold higher than that observed in the intraorbital segment (~100 N/m² at the same time point). Notably, comparable stress concentration patterns were consistently observed in simulations of superior, inferior, and nasal periorbital impacts (Fig. S1), collectively identifying the intracanalicular segment as the primary biomechanical weak point during blunt orbital trauma.

Direct optic canal impact caused little collateral injury and showed robustness against bias

Given the finite element analyses identifying the intracanalicular segment as the primary biomechanical vulnerability, two injury paradigms were considered for modeling TON: (i) indirect periorbital impact, in which external blunt force is transmitted to the optic canal through the orbital bones; and (ii) direct impact targeted to the optic canal itself. To determine which strategy provides superior safety and mechanical robustness, finite element analysis was used to compare these two approaches.

Simulations of indirect periorbital impact revealed widespread dispersion of mechanical forces across the maxillary bone, nasal bone, and skull base (Fig. 3A, B).

In contrast, direct optic canal impact caused minimal force propagation to adjacent skull structures (Fig. 3C, D), while producing a force distribution pattern along the optic nerve comparable to that induced by periorbital impact (Fig. 3E, F). Notably, direct optic canal impact required a substantially lower input force of 195 N, corresponding to approximately 5% of that used for temporal periorbital impact (3900 N), to achieve a similar peak force density

446 within the intracanalicular segment (Fig. 3F), thereby reducing the likelihood of off-target
447 skeletal injury.
448 Importantly, direct optic canal impact also demonstrated greater robustness against bias than
449 indirect periorbital impact. Specifically, compared with indirect periorbital impact, a 10°
450 deviation from the optimal vertical impact angle (Fig. 3G,H,J,K), as well as a 10% variation in
451 bone mechanical properties, including density, Young's modulus, and Poisson's ratio (Fig.
452 3I,L), resulted in only minor fluctuations in force distribution along the intracanalicular optic
453 nerve following direct optic canal impact.
454 Collectively, these results demonstrated that direct optic canal impact induces optic canal–
455 centered injury with minimal collateral damage and high robustness against bias.
456
457 **Goat model recapitulates human finite-element results**
458 Goats are a highly suitable experimental species because their paranasal sinus anatomy closely
459 resembles that of humans, facilitating minimally invasive transnasal endoscopic access to the
460 optic canal. Additionally, compared with other large-animal models, goats are more cost-
461 effective and readily available(Zhang et al., 2022). To further validate Saanen goats as an
462 appropriate large-animal translational model, we performed goat-specific finite-element
463 analysis (FEA) based on high-resolution micro-CT scans of the skull (Figure S2A, B).
464
465 Notably, the mechanical stress transmission pattern observed in the goat model closely
466 mirrored that of human simulations. Following direct impact, mechanical stress was primarily
467 concentrated in the intracanalicular segment of the optic nerve (Figures S2C, S2E).
468 Quantitative analysis revealed that 90.91% of the total von Mises stress was localized to the
469 directly impacted optic canal segment (Figure S2F). Consistent with human simulations,
470 regional impact quantification confirmed the high safety of this approach in goats: the optic

canal absorbed the majority of the applied force (normalized ratio = 100%), while adjacent structures—the maxilla (4.52%), nasal cavity (1.1%), and skullbase (1.33%)—experienced minimal mechanical transmission (Figures S2D).

These goat-specific data demonstrate the biomechanical equivalence of the model to human simulations and establish the safety and precision of directly impacting the optic canal for subsequent in vivo studies.

A reproducible goat TON model with optic canal fracture is established by direct optic canal impact under transnasal endoscopy

Based on the finite element analysis results, we identified direct optic canal impact as a more robust injury paradigm and first engineered a gas-driven impactor to experimentally recapitulate TON. This device employed high-pressure air to propel an impact rod forward by 2 mm, thereby inducing an optic canal fracture with impinged bone (Fig. 4A–C). The air pressure within the storage chamber was manually adjustable from 1 to 10 megapascals (MPa), with higher pressures generating greater impact forces (Fig. 4B). An operating pressure of 3 MPa was selected, as it produced more consistent impact forces compared with lower (2 MPa) or higher (4 MPa) pressure settings (Fig. 4B).

We chose goat as an ideal model for TON. Under endoscopic visualization, the middle turbinate, nasal septum, and olfactory nerve bundles were sequentially resected using a straight-cut microdebrider or scissor (Fig. 4E-a,b,c), thereby exposing the anterior wall of the sphenoid bone, which exhibited a characteristic inverted heart-shaped appearance and served as a key anatomical landmark (Fig. 4E-d). The anterior cortical bone of the sphenoid was then carefully drilled to open the sphenoid cavity and create an artificial sphenoid sinus (Fig. 4E-e,f,g,h). Further bone removal within the artificial sphenoid sinus was performed using a diamond microdrill, which progressively widened the surgical corridor and allowed clear

visualization of the optic canal within the operative field (Fig. 4E-i). The impact device was subsequently advanced along the predefined trajectory and precisely positioned against the anterior wall of the optic canal under endoscopic guidance (Fig. 4E-j). Upon triggering the impactor, a displaced, impacted optic canal fracture with inwardly displaced bone fragments was immediately observed under endoscopic visualization, resulting in direct compression of the intracanalicular optic nerve (Fig. 4E-k). Follow-up computed tomography (CT) imaging further confirmed that the fracture morphology closely resembled that observed in patients with TON (Fig. 1A, 4F).

Structural damage to retinal ganglion cells was quantified by OCT. In the injured eyes, peripapillary ganglion cell complex (GCC) thickness exhibited significant thinning across all measured macular sectors (NS, N, NI, TI, T, and TS). For instance, in the temporal-superior (TS) sector, the GCC thickness decreased from 323.4 ± 76.1 μm at baseline to 286.5 ± 67.8 μm at 1 month post-injury (1 mpi), corresponding to a ~11.4% reduction ($P = 0.0018$, two-way ANOVA, time factor; Fig. 5A,B), whereas GCC thickness in the contralateral eyes remained unchanged (Fig. S4A), indicating preservation of retinal structure in the fellow eye.

Functionally, the direct pupillary light reflex (dPLR) in the injured eye and the indirect PLR (iPLR) in the contralateral eye were both markedly reduced over time (Fig. 5C, D). In contrast, the dPLR in the contralateral eye and the iPLR in the injured eye remained intact (Fig. S4B). This dissociated PLR pattern met the predefined criteria for a relative afferent pupillary defect (RAPD) (Soleimani et al., 2011). Electrophysiological assessments showed consistent functional deficits in the injured eyes across all tested stimulus conditions. For instance, at a flash intensity of 0.25 cd·s/m², the FVEP P1–N1 amplitude ratio (injured/contralateral) decreased from 1.020 ± 0.306 at baseline to 0.573 ± 0.229 at 1 mpi (≈ 43.8% reduction; $P = 0.0010$; Fig. 5E, F). Similarly, across all tested spatial frequencies (0.1 – 3.0 cpd), the PERG P1 – N1 amplitude ratio demonstrated significant declines. At 0.3 cpd, this ratio

declined from 1.113 ± 0.444 to 0.528 ± 0.124 at 1mpi (≈52.6% reduction; $P < 0.0001$; Fig. 5G, H). In the contralateral uninjured eyes, FVEP and PERG amplitudes did not show significant changes compared with baseline (Fig. S4C, D).

Together, these results showed that transnasal endoscopic direct optic canal impact produced optic canal fracture and unilateral structural and functional deficits in goats. We then implemented a second-generation elastic-energy driven device for subsequent experiments.

Elastic-energy–driven impact system for optic canal fracture modeling

To this end, we developed a second-generation elastic-energy driven, spring-based impact device for inducing optic canal fracture with impinged bone (Fig. 6A). The system employs a compression spring with dimensions of 1.5 × 12 × 45 mm, in which the deformation length is positively correlated with the delivered impact force (Fig. 6B). Based on mechanical calibrations (Fig. S3B, S3C), a deformation length of 20 mm was selected to generate an impact force equivalent to that produced by the gas-driven device at 3 MPa, thereby maintaining comparable injury severity while eliminating pneumatic instability. To further ensure highly localized and reproducible energy delivery, dynamic kinetic characterization was performed. The temporal impulse waveform confirmed a tightly controlled mechanical stimulus with a restricted dwell time of 4.0 ms (Fig. S3A). Additionally, standardized quantitative engineering specifications were established for the impactor system, which utilizes a 2.0 mm rod tip diameter, a strictly restricted 2.0 mm mechanical stroke length, and a derived peak impact velocity of 2.0 m/s at the point of tissue contact (Fig. S3D).

To further enhance precision and reproducibility in large-animal procedures, a motorized stabilizing base incorporating five independently actuated joints was constructed (Fig. 6C). This configuration effectively counteracted recoil during impact and enabled multi-axis

positional adjustment (Fig. 6D), converting the system from a handheld device into a mechanically stabilized platform and substantially improving targeting accuracy.

Following fracture induction with the modified device, transnasal endoscopic examination revealed a circular bony fragment displaced into the optic canal lumen, while corresponding sagittal CT imaging confirmed fracture of the anterior wall of the optic canal at the impact site (Fig. 6E).

Structural assessment by OCT demonstrated significant thinning of the peripapillary ganglion cell complex (GCC) across all measured macular sectors in the injured eyes. For instance, in the temporal-superior (TS) sector, GCC thickness decreased from 336.2 ± 58.2 μm at baseline to 249.2 ± 39.8 μm at 1 mpi, representing an ~25.9% reduction ($P = 0.00022$; Fig. 6F,G), whereas no significant thinning was detected in the contralateral eyes (Fig. S5A). These structural changes were comparable to those observed following gas-driven impact, indicating preserved injury severity. Consistent with structural damage, functional assessments revealed unilateral visual deficits. Both the indirect pupillary light reflex (iPLR) in the injured eye and the direct PLR (dPLR) in the contralateral eye remained intact (Fig. S5B), whereas the dPLR in the injured eye was abolished and that in the contralateral eye was preserved (Fig. 6H, I). Electrophysiological measurements again revealed unilateral functional impairment. In the injured eyes, for instance, at a flash intensity of 0.25 cd·s/m², the FVEP P1–N1 amplitude ratio decreased from 1.086 ± 0.323 at baseline to 0.321 ± 0.158 at 1 mpi (≈70.4% reduction; $P < 0.0001$; Fig. 6J,K). Similarly, at a spatial frequency of 0.3 cpd, the PERG P1–N1 amplitude ratio declined from 1.215 ± 0.489 at baseline to 0.513 ± 0.068 at 1mpi (≈57.8% reduction; $P < 0.0001$; Fig. 6L, M). In contrast, no significant reductions in FVEP or PERG amplitudes were observed in the contralateral eyes compared with baseline values (Fig. S5C, D), confirming a unilateral deficit without widespread bilateral involvement.

Localized impact induces profound retrograde retinal ganglion cell loss and intracanalicular axonal degeneration

To validate the biological consequences of the mechanical stress channeling predicted by our caprine FEA model, we evaluated the survival of retinal ganglion cells (RGC) and the structural integrity of the optic nerve at 1 month post-injury (1mpi).

We first assessed the survival of RGC within the retina to determine the extent of impact-induced retrograde degeneration. Whole-mount retinal immunofluorescence staining for RBPMS revealed a densely packed distribution of RGC in the uninjured contralateral (Control) eyes, whereas the traumatized (Injury) eyes exhibited widespread and diffuse RGC loss (Figure 7A). Standardized quantification across the mid-peripheral retina confirmed a statistically significant reduction in RGC survival in the impacted group compared to the intra-animal controls (Figure 7B, $P < 0.05$).

To elucidate the primary mechanical insult driving this retrograde RGC death and driven by our computational prediction that impact stress predominantly concentrates within the intracanalicular segment of the optic nerve, we subsequently performed high-resolution paraphenylenediamine (PPD) staining on cross-sections from this specific anatomical locus. The control nerves displayed typical healthy morphology, characterized by tightly packed axons enveloped by thick, uniform, and intact myelin sheaths (Figure 7C, left). In striking contrast, the injured nerves demonstrated classic hallmarks of severe Wallerian-like degeneration, including massive intra-axonal vacuolization, extensive myelin sheath disruption, and structural collapse (Figure 7C, right). Quantitative assessment corroborated these qualitative observations, revealing a catastrophic and highly significant depletion of viable axons within the intracanalicular segment of the impacted group (Figure 7D, $P < 0.01$).

Taken together, these robust in vivo cellular and microstructural findings perfectly mirror the classical pathological cascade of clinical TON, thereby providing definitive biological validation for the compressive injury mechanism elucidated by our biomechanical model.

Discussion

Why optic canal–centered biomechanics matter for modeling TON

TON is widely recognized as a consequence of blunt cranio-orbital trauma, and clinical and radiological studies have long implicated the optic canal as a frequent site of injury, particularly in cases accompanied by optic canal fracture. Although optic canal's anatomical vulnerability is recognized, the precise biomechanical pathways of force transmission remain poorly characterized. Specifically, how external forces propagate through the cranio-orbital skeleton and concentrate on the intracanalicular optic nerve is unclear. This lack of quantitative understanding has limited the development of biofidelic experimental models.

In particular, existing TON models have largely been defined by empirical injury paradigms rather than by clinically informed mechanical criteria. As a result, although many models reproduce downstream pathological outcomes, such as RGC loss or visual dysfunction, the biomechanical fidelity of injury induction, especially with respect to optic canal involvement, has been difficult to assess in a standardized and quantitative manner. Consequently, a gap remains between clinically observed optic canal–centered injury patterns and the experimental frameworks used to model TON.

In this study, we addressed this gap by reconstructing a high-resolution human head finite element model to quantitatively characterize force transmission during clinically relevant blunt impacts. Our analyses mapped stress propagation and demonstrated preferential stress convergence within the intracanalicular segment. However, it should be further emphasized

617 that these simulation results are not formal clinical validations, but rather validations of the
618 apparent validity of our biomechanical assumptions.
619 Importantly, these computational simulations were primarily used to clarify macroscopic
620 biomechanical pathways and to guide the design and parameters of our transnasal impactor.
621 They do not provide direct evidence of optic nerve degeneration. Definitive validation of the
622 TON model relies on our subsequent in vivo structural, functional, and histological assessments.
623 We determined that direct optic canal impact represents a biofidelic injury paradigm for TON.
624 Implemented under transnasal endoscopic guidance in goats, this approach enables controlled
625 induction of optic canal fracture and intracanalicular nerve compression while preserving the
626 surrounding ocular structures. In doing so, the model establishes not only anatomical and
627 pathological similarity to human TON, but also a quantitative link between biomechanics and
628 experimental injury induction, providing a more rigorous framework for evaluating disease
629 severity and therapeutic intervention.
630 From a structural mechanics perspective, the intracanalicular segment is uniquely susceptible
631 to load convergence because it is constrained within a rigid bony canal and surrounded by
632 tightly apposed meningeal and periosteal interfaces (Pircher et al., 2017), leaving limited
633 capacity for displacement or stress redistribution during cranio-orbital impact. Under blunt
634 trauma, forces transmitted along the orbital walls can therefore be funneled toward the optic
635 canal and translated into localized compression and shear on the intracanalicular nerve. This
636 anatomical confinement provides a plausible mechanistic explanation for why the peak loading
637 in our simulations consistently emerged at the intracanalicular segment across multiple impact
638 directions. Importantly, this biomechanical information helps connect experimental TON
639 model to a clinically relevant injury pattern and offers quantitative parameters that can be used
640 to standardize injury severity across studies.
641

Comparison with existing TON models

Most existing TON models rely on rodents and direct optic nerve crush (Tang et al., 2011). While these approaches reliably induce RGC loss and visual dysfunction, they bypass the optic canal and thus fail to reproduce the canal fracture–mediated injury characteristic of human TON. Additionally, crush injuries are typically applied to the retrobulbar segment near the globe, causing rapid retrograde degeneration and early RGC apoptosis—dynamics that differ from human TON, where injury occurs within the optic canal. Consequently, the temporal progression of RGC degeneration and visual dysfunction in crush models may not accurately reflect clinical patterns, limiting their ability to replicate optic canal fracture–mediated pathology.

More invasive rodent models, such as optic tract transection following craniotomy, allow precise manipulation of post-chiasmatic injury but require extensive cranial opening, introducing surgical trauma and systemic stress. Ultrasound-based paradigms (Tao et al., 2017) partially mimic blunt orbital impact but deposit energy in surrounding soft tissues, often causing collateral damage to extraocular muscles, eyelids, or bone. The TITON model developed by Ryan et al. isolates shear forces via torsional injury, highlighting the utility of rodents for specific biomechanical studies(Ryan et al., 2025). However, rodents have open orbits and extremely short optic canals, unlike the deep, enclosed human canal, limiting the translation of stress transmission and force-funneling dynamics. While these models capture important aspects of optic nerve injury, they do not replicate the combination of canal fracture, localized intracanalicular compression, and contralateral eye preservation seen in many human TON cases.

In contrast, our goat model was explicitly designed to reflect human-relevant biomechanics. Grounded in human-head finite-element analysis and implemented via a minimally invasive transnasal approach, it preserves the optic canal–centered injury mechanism. Goats' cranio-

orbital anatomy and optic canal geometry closely resemble humans, enabling realistic force transmission and improved biomechanical fidelity. The relatively larger surgical space around the optic canal allows endoscopic manipulation, device deployment, and interventional refinement, creating opportunities for therapeutic and surgical technology development not feasible in murine models. Together, these features position the goat optic canal fracture model as a biofidelic platform bridging small-animal studies and human disease, offering clear advantages for mechanistic and preclinical research. Importantly, rather than replacing existing rodent TON paradigms, this large-animal model complements them by providing human-relevant biomechanical fidelity and an experimental platform for interventions that are not feasible in small animals.

Inter-species biomechanical considerations

While Saanen goats provide an anatomically favorable platform for trans-nasal endoscopic access to the pre-chiasmatic optic nerve, translating caprine biomechanical findings to humans necessitates careful consideration of inter-species morphometric differences. Goat cranial bone density, absolute optic canal dimensions, and periorbital soft tissue thicknesses differ from human parameters. Nevertheless, comparative finite-element analysis (FEA) demonstrates that the fundamental mechanism of indirect TON is governed primarily by conserved topological architecture rather than absolute anatomical scaling. In both humans and goats, the optic canal forms a rigid, narrow bony “choke point” surrounding the viscoelastic optic nerve. The extreme stiffness mismatch between cortical bone and neural tissue—spanning several orders of magnitude—ensures that dynamic mechanical stress from periorbital impact is funneled into the intracanalicular segment. As a result, despite macroscopic morphological differences, highly localized stress concentrations and subsequent axonal injury patterns are faithfully recapitulated in the caprine model.

Sequential phenotype of the goat TON model

The traumatic optic neuropathy (TON) phenotype in this caprine model emerges in a clearly defined temporal sequence. An acute functional deficit, manifested as a relative afferent pupillary defect (RAPD), is detectable within 24 hours post-impact, serving as an immediate indicator of successful model induction. Progressive structural degeneration, including retinal ganglion cell complex (GCC) thinning, along with severe electrophysiological deficits reflected in FVEP and PERG amplitude reductions, are definitively observed at one month post-injury. These sequential manifestations underscore the translational value of the model, complementing existing rodent paradigms by offering unique biomechanical and anatomical advantages without replacing smaller-scale models.

Synergistic contribution of primary and secondary injury mechanisms

Pathophysiologically, the progressive neuropathy observed in this model is the result of synergistic interactions between primary and secondary injury mechanisms. The initial mechanical shock delivers substantial kinetic energy to the intracanalicular optic nerve, likely causing immediate axonal contusion and shearing. Subsequently, the reproducibly generated depressed fracture fragment exerts sustained physical compression, initiating secondary ischemic and neuroinflammatory cascades that culminate in progressive retinal ganglion cell apoptosis over the one-month follow-up period. While the current study design does not allow quantitative separation of primary versus secondary contributions, and the specific molecular mechanisms driving these secondary pathological changes require further exploration via future multi-omics analyses, the reproducible creation of a stable, space-occupying fracture fragment closely mirrors clinical compressive TON. This feature renders the model uniquely suitable for preclinical studies evaluating the timing, technique, and efficacy of endoscopic decompression strategies.

Advantages of the optimized elastic-energy driven impactor

Accurate and reproducible induction of optic canal injury is critical for large-animal modeling of traumatic optic neuropathy (TON). In this study, we refined the initial gas-driven impact system into a second-generation elastic-energy–driven impactor to overcome limitations inherent to pneumatic actuation. While the gas-driven device enabled initial validation of transnasal endoscopic access and impact-induced visual dysfunction, its performance was constrained by several operational factors. High-pressure pneumatic operation imposed stringent requirements on sealing and component durability, and repeated use led to wear, occasional air leakage, and reduced long-term robustness. Variations in cylinder pressure caused fluctuations in output force, compromising the consistency of optic canal fracture induction, while mechanical recoil and handheld operation limited spatial precision and increased operator-dependent variability.

The elastic-energy–driven system addresses these challenges by delivering a deterministic, spring-mediated energy transfer governed by Hooke's law, resulting in highly reproducible peak forces and consistent loading rates. Its design allows precise control of dwell time and a sharp deceleration phase, minimizing secondary reverberations and residual compression typically observed in gas-driven devices. Integration with a multi-joint motorized stabilizing base further enhances positional stability and virtually eliminates operator-dependent variability. Together, these refinements create a robust, reproducible, and scalable platform capable of producing consistent optic canal fractures across different surgical postures and large-animal species. By combining reliability, precision, and ease of standardization, the optimized elastic-energy–driven impactor represents a substantial advance for mechanistic studies and preclinical testing of TON.

Limitations and outlook

Despite the advantages of this model, several limitations must be considered when interpreting the results and planning future studies.

1. Simplified Finite-Element Analysis

Regarding finite-element analysis (FEA), our model assumed isotropic and homogeneous material properties and did not incorporate vascular structures or intracranial soft tissues, such as cerebrospinal fluid (CSF) and brain parenchyma. This simplification was primarily necessitated by the limited resolution of clinical CT imaging, which precluded precise segmentation of vascular and CSF interfaces for detailed three-dimensional reconstruction. In addition, the subarachnoid space within the human optic canal is extremely narrow, with minimal CSF volume and limited free flow (Liugan et al., 2017), rendering the hydraulic damping effect within the bony canal negligible. Furthermore, although assuming isotropy may affect precise local stress estimates within the anisotropic axonal tracts, the massive stiffness gradient between the rigid craniofacial skeleton (GPa range) and neural tissues (kPa range) ensures that the macroscopic spatial pattern of stress convergence toward the optic canal is fundamentally driven by skeletal deformation. This stiffness-dominated macroscopic response aligns with established biomechanical paradigms in recent TON modeling(Li et al., 2020), confirming that our model's stress routing remains robust despite soft-tissue simplifications. Finally, relying on generalized mammalian biomechanical constants rather than caprine-specific ex vivo mechanical testing remains an additional limitation.

2. Sample Size, Statistical Power, and Inter-Individual Variability

Large-animal studies inherently require substantial logistical and financial resources, which constrain achievable sample sizes compared with rodent models. To ensure rigorous validation and address potential concerns regarding generalizability, we conducted a comprehensive post hoc power analysis for the primary endpoints (Table S3). The analysis confirmed that, with a

767 relatively small sample size, the calculated statistical power for both structural (OCT) and
768 functional (FVEP, PERG) endpoints consistently exceeded 85%, demonstrating
769 mathematically that our current cohort is sufficient to robustly capture the core phenotypic
770 features of the model.

771 However, it should be acknowledged that, although our sample size provides adequate power
772 to validate the observed structural and functional deficits, it may be underpowered for detecting
773 subtle biological or molecular differences. To overcome this limitation, future studies may
774 incorporate larger cohorts of large animals to enable detection of finer-scale biological effects.
775 Inter-individual cranio-orbital variability also warrants consideration. The robustness of the
776 impact site against anatomical differences is supported by our simulations (Fig. 3), which show
777 that even with ±10° deviations in impact angle or ±10% variation in bone mechanical properties
778 (density, Young's modulus, Poisson's ratio), the optic nerve within the canal consistently
779 experiences the highest localized mechanical stress. This demonstrates that the impactor design
780 and targeting strategy are inherently resistant to minor anatomical or procedural variations,
781 ensuring reproducible force delivery across subjects. Additionally, strict age- and weight-
782 matching of experimental animals further reduces baseline variability.

783 3. Sex Selection

784 This foundational study used a uniform, single-sex cohort of male goats. This approach was
785 chosen to minimize confounding effects from female estrous cycle–related hormonal
786 fluctuations (e.g., estrogen and progesterone), which can exert potent and variable
787 neuroprotective and immunomodulatory effects following neurotrauma. Furthermore, this
788 selection closely aligns with the clinical epidemiology of TON, which overwhelmingly affects
789 males due to higher rates of severe craniofacial trauma, as confirmed by our recent large-scale
790 clinical survey(Zhang et al., 2025). By mirroring the primary clinical demographic, the use of
791 male-only animals ensured reproducibility of macroscopic structural and functional outcomes

while adhering to ethical 3Rs guidelines (reduction) for large-animal research. We explicitly acknowledge that this design inherently limits the evaluation of sex as a biological variable. Future studies will incorporate mixed-sex cohorts with larger sample sizes to enhance generalizability.

4. Surgical Approach and Local Inflammation

We acknowledge that the creation of an artificial sphenoid sinus inherently induces a certain degree of local surgical trauma. However, owing to the minimally invasive nature of our transnasal endoscopic approach, only the essential and minimal mucosal resection is performed, which substantially limits the local inflammatory response. Furthermore, in previous studies, sham-operated control animals that underwent identical surgical exposure without optic nerve injury exhibited no significant structural or functional visual deficits (Zhang et al., 2022). Combined with observations of the contralateral, uninjured eyes in the current study, these findings indicate that secondary local inflammation did not produce detectable structural or functional effects in the fellow eyes. Nevertheless, recent large-scale clinical surveys report that 3.7% of TON patients present with bilateral involvement (Zhang et al., 2025), suggesting that subtle systemic neuroinflammatory or trans-synaptic central effects on the contralateral eye cannot be entirely excluded.

5. Diagnostic Criteria and Selection Bias

The large-animal TON model established in this study does not involve quantitative grading of optic canal injury. To minimize variability and avoid inclusion of animals with mild or delayed functional deficits, we selected a stringent inclusion criterion based on the most severe TON injury: a RAPD grade difference ≥2 within 24 hours. While this approach ensures consistency of baseline injury for subsequent intervention studies, it may limit the model’s representation of the full clinical spectrum of TON.

6. Short Post-Injury Follow-Up

While one-month post-injury assessments provide sufficient validation of the acute and subacute model, extended follow-up will be required to delineate chronic neurodegenerative changes and to determine whether subtle bilateral compensatory or inflammatory effects occur over time.

Conclusion

By combining high-resolution human head finite element analysis with iterative engineering refinement, we identified the intracanalicular segment of the optic nerve as the principal biomechanical vulnerability during blunt periorbital trauma and leveraged this insight to establish a biofidelic, transnasal endoscopic optic canal fracture model in goats. This large-animal model reproducibly recapitulates the defining structural and functional features of clinical TON, including optic canal fracture, GCC thinning, relative afferent pupillary defect, visual electrophysiological deficits and definitive RGC and axonal degeneration, while minimizing collateral injury and preserving the fellow eye. Building on this framework, the goat model and elastic-energy–driven impact system provide a practical platform for future studies on neuroprotection, axonal regeneration, surgical decompression strategies, and the development of translational interventions targeting optic canal–centered traumatic optic neuropathy. Ultimately, this model and the associated impact system provide a rigorously standardized preclinical platform for future translational investigations of neuroprotective therapies, axonal regeneration, and surgical decompression strategies.

Data availability

Data and code will be made available on reasonable request.

Competing interests

The authors declare no competing interests.

Author contributions

Conceptualization: Y.Z., W.W., Z.Y.; Data curation: Z.Y., Y.Z.; Formal analysis: H.D., T.Y.; Funding acquisition: W.W., Y.Z.; Investigation: Z.Y., Y.Z., H.D., T.Y., Y.C., S.T., B.X., T.X., H.W., S.L., M.L., S.Z., H. C., S.H., J.Z., Y.W., R.Z.; Methodology: Z.Y., T.Y., Y.C., S.T.; Project administration: Y.Z., Z.Y.; Resources: W.W., Y.Z.; Supervision: Y.Z., W.W., J.Y.; Visualization: Z.Y., T.Y.; Writing – original draft: Z.Y., T.Y.; Writing – review & editing: Y.Z., W.W., J.Y..

Acknowledgements

We gratefully acknowledge the support of the large-animal housing and care platform at Wenzhou Medical University for providing husbandry and veterinary assistance throughout this study. We thank Zhongshi Technology Co., Ltd. for their assistance in designing and manufacturing the customized impact devices used in this study.

Funding

This work was supported by: the National Key R&D Program of China (Grant No.2022YFA1105500), the Key Science and Technology Program of Wenzhou (Grant No.ZY2022021) and the National Natural Science Foundation of China (Grant No.82471080).

References

Benowitz LI, He Z, Goldberg JL (2017) Reaching the brain: Advances in optic nerve regeneration. Experimental Neurology. 287:365–373

Chen B, Zhang H, Zhai Q, et al. (2022) Traumatic optic neuropathy: a review of current studies. Neurosurgical Review. 45:1895–1913

Chen Y, Ostoja-Starzewski M (2010) MRI-based finite element modeling of head trauma: spherically focusing shear waves. Acta Mechanica. 213:155–167

Crompton MR (1970) VISUAL LESIONS IN CLOSED HEAD INJURY. Brain. 93:785–792

Gise R, Truong T, Parsikia A, et al. (2018) Visual Pathway Injuries in Pediatric Ocular Trauma—A Survey of the National Trauma Data Bank From 2008 to 2014. Pediatric Neurology. 85:43–50

Huempfner-Hierl H, Bohne A, Wollny G, et al. (2015) Blunt forehead trauma and optic canal involvement: finite element analysis of anterior skull base and orbit on causes of vision impairment. British Journal of Ophthalmology. 99:1430–1434

Ibrahim AS, Elmasry K, Wan M, et al. (2018) A Controlled Impact of Optic Nerve as a New Model of Traumatic Optic Neuropathy in Mouse. Investigative Opthalmology & Visual Science. 59:5548

Laha B, Stafford BK, Huberman AD (2017) Regenerating optic pathways from the eye to the brain. Science. 356:1031–1034

Lee J, Nguyen S, Bhattacharya S (2024) Optic nerve regeneration: Potential treatment approaches. Current Opinion in Pharmacology. 74:102428

Li Y, Singman E, McCulley T, et al. (2020) The Biomechanics of Indirect Traumatic Optic Neuropathy Using a Computational Head Model With a Biofidelic Orbit. Frontiers in Neurology. 11:346

Liugan M, Xu Z, Zhang M (2017) Reduced Free Communication of the Subarachnoid Space Within the Optic Canal in the Human. American Journal of Ophthalmology. 179:25–31

Maire E, Withers PJ (2014) Quantitative X-ray tomography. International Materials Reviews. 59:1–43

Pircher A, Montali M, Berberat J, et al. (2017) The Optic Canal: A Bottleneck for Cerebrospinal Fluid Dynamics in Normal-Tension Glaucoma? Frontiers in Neurology. 8

Ryan AK, Asemota BI, Heisler-Taylor T, et al. (2025) Torsion-Induced Traumatic Optic Neuropathy (TITON): A physiologically relevant animal model of traumatic optic neuropathy. PLOS ONE. 20:e0312220

Soleimani M, Tabatabaei, Alami, et al. (2011) Predictive value of visual evoked potentials, relative afferent pupillary defect, and orbital fractures in patients with traumatic optic neuropathy. Clinical Ophthalmology. 1021

Tang Z, Zhang S, Lee C, et al. (2011) An Optic Nerve Crush Injury Murine Model to Study Retinal Ganglion Cell Survival. Journal of Visualized Experiments. 2685

Tao W, Dvoriantchikova G, Tse BC, et al. (2017) A Novel Mouse Model of Traumatic Optic Neuropathy Using External Ultrasound Energy to Achieve Focal, Indirect Optic Nerve Injury. Scientific Reports. 7:11779

913 Tsai NY, Gallo RA, Pelaez D, et al. (2024) Traumatic Optic Neuropathy: Challenges and
914 Opportunities in Developing Neuroprotective and Neuroregenerative Therapies.
915 Current Ophthalmology Reports. 12:23–29

916 Wu W, Selva D, Bian Y, et al. (2015) Endoscopic Medial Orbital Fat Decompression for
917 Proptosis in Type 1 Graves Orbitopathy. American Journal of Ophthalmology.
918 159:277–284

919 Yu-Wai-Man P (2015) Traumatic optic neuropathy—Clinical features and management
920 issues. Taiwan Journal of Ophthalmology. 5:3–8

921 Zhang Y, Li M, Yu B, et al. (2022) Cold protection allows local cryotherapy in a clinical-
922 relevant model of traumatic optic neuropathy. eLife. 11:e75070

923 Zhang Y, Sun J, Ye Q, et al. (2021) In vivo evaluation of outer retinal function and structure
924 after retrobulbar optic nerve crush by lateral orbitotomy in goats. Experimental Eye
925 Research. 209:108652

926 Zhang YiKui, Xu B, Huang ShiWei, et al. (2025) Large-scale survey, animal models, and
927 computational modeling identify histological neurodegenerative biomarkers for
928 traumatic optic neuropathy. JCI Insight. 10:e190682

929

930
931
932
933
934
935
936
937
938
939
940

941 **Table 1 Material properties.**

tissue	density (kg/ m³)	Material parameters
optic nerve	1040	E_∞=30kPa，ν~0.5; g_1=0.45,τ_1=0.5;g_2=0.365 τ_2=50
skull	1300	E=14.5GPa，ν=0.35
eyeball	1006	K=2.272GPa，ν~0.5
extraocular muscles	1200	E=11MPa，ν=0.4
ligament	1109	E=5MPa，ν=0.4

942
943
944
945
946
947
948
949
950
951
952
953
954
955
956
957

Figures

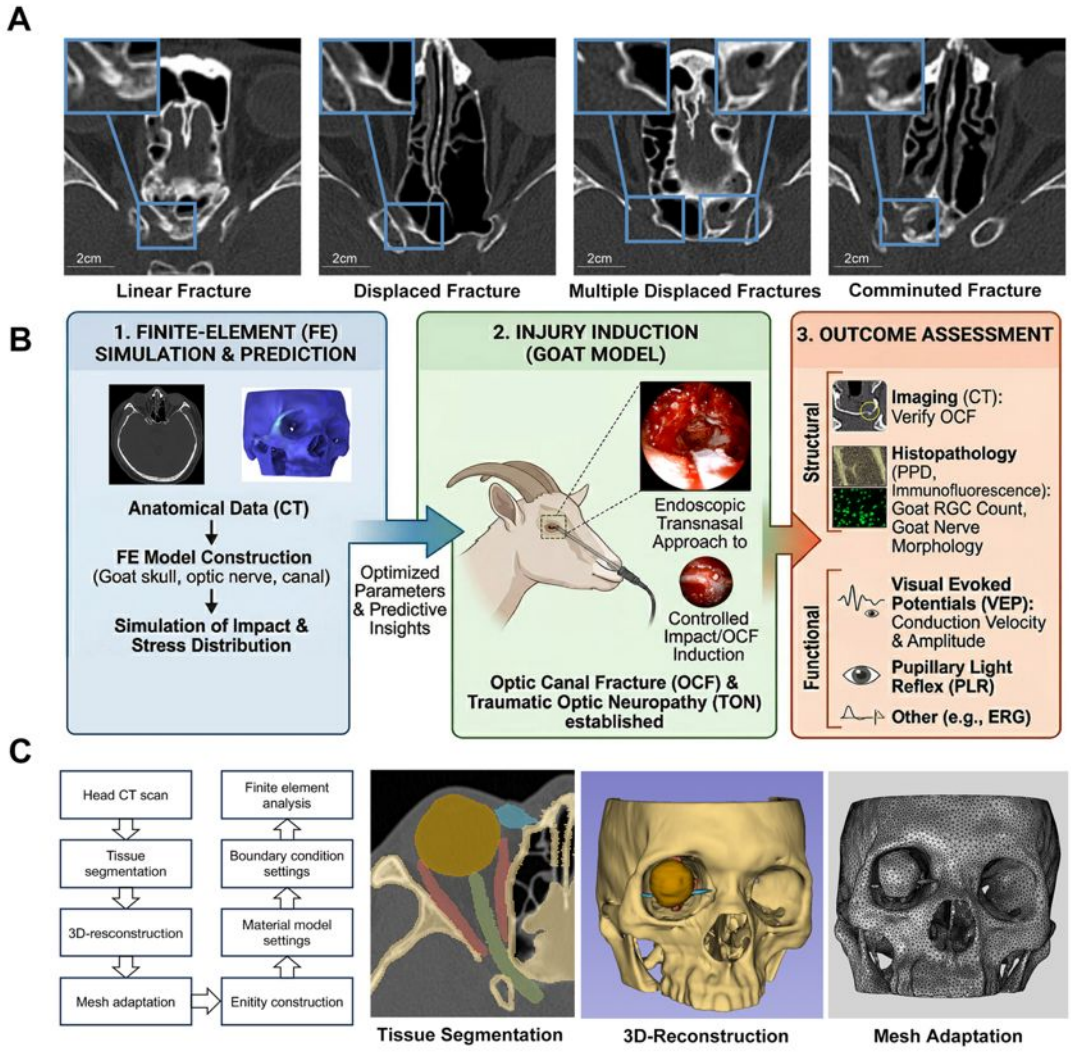

Figure 1 Finite element model of the human head used to simulate force transmission to the optic canal.

(A) Representative horizontal head CT images depicting various optic canal fractures in clinical TON cases. Scale bar = 2cm

(B) A concise schematic summarizing the overarching research workflow, progressing from computational biomechanical simulation to in vivo injury induction and subsequent biological validation.

(C) Flowchart and representative images demonstrating finite element analysis based on head CT scan step by step, including tissue segmentation, 3D-reconstruction, and mesh adaptation.

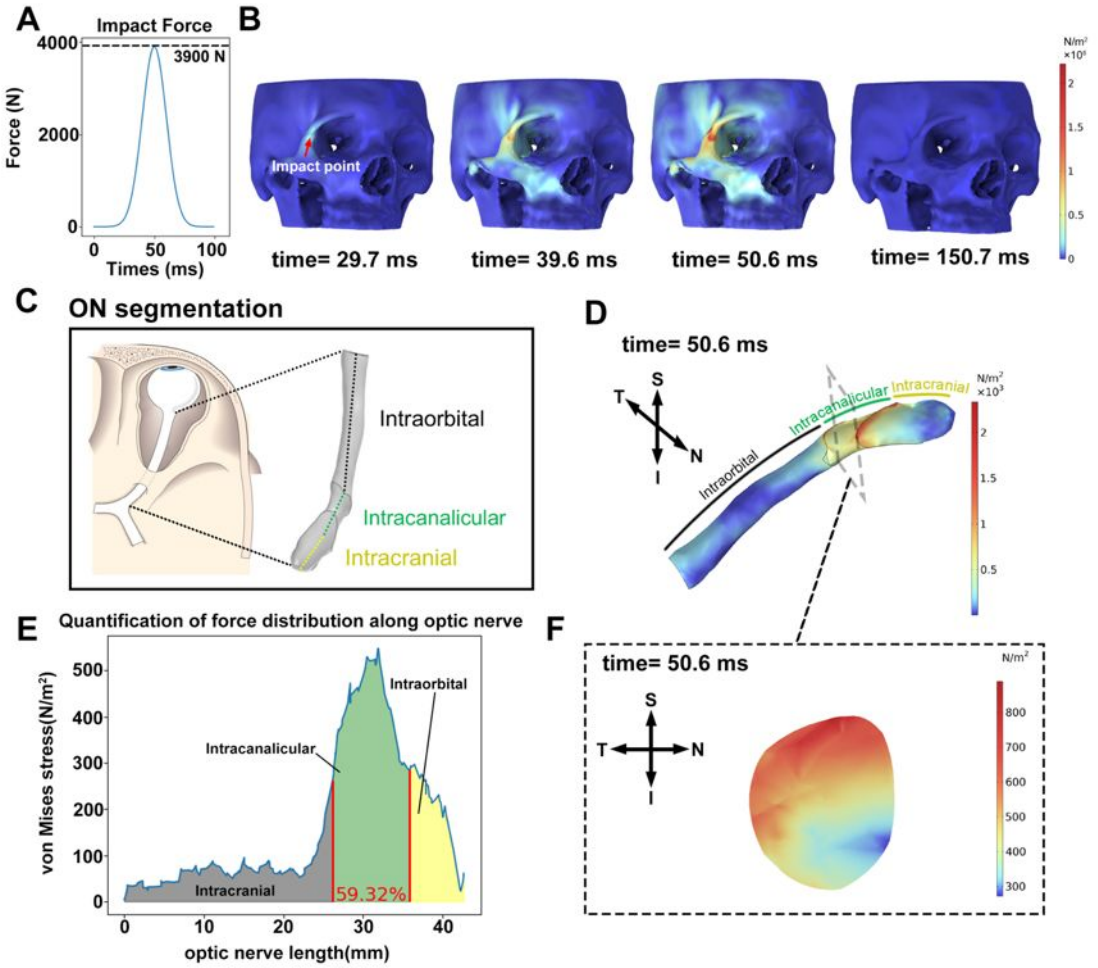

969

970 **Figure 2 The intracanalicular optic nerve suffered the highest mechanical stress**

971 **following a periorbital blunt impact.**

972 **(A)** Impact force reached its peak at 50 ms, exhibiting a Gaussian distribution with a magnitude

973 of 3900 N.

974 **(B)** Color-coded displays showing force propagation from the periorbital region towards the

975 optic canal along the orbital wall.

976 **(C)** Anatomic segmentation of the optic nerve (ON).

977 **(D-E)** Color-coded illustration and quantification of force distribution along the ON at 50.6

978 ms.

(F) Cross-sectional stress map showing the force distribution at the center of the intracanalicular segment of the optic nerve at 50.6 ms. S: Superior, I: Inferior, N: Nasal, T: Temporal.

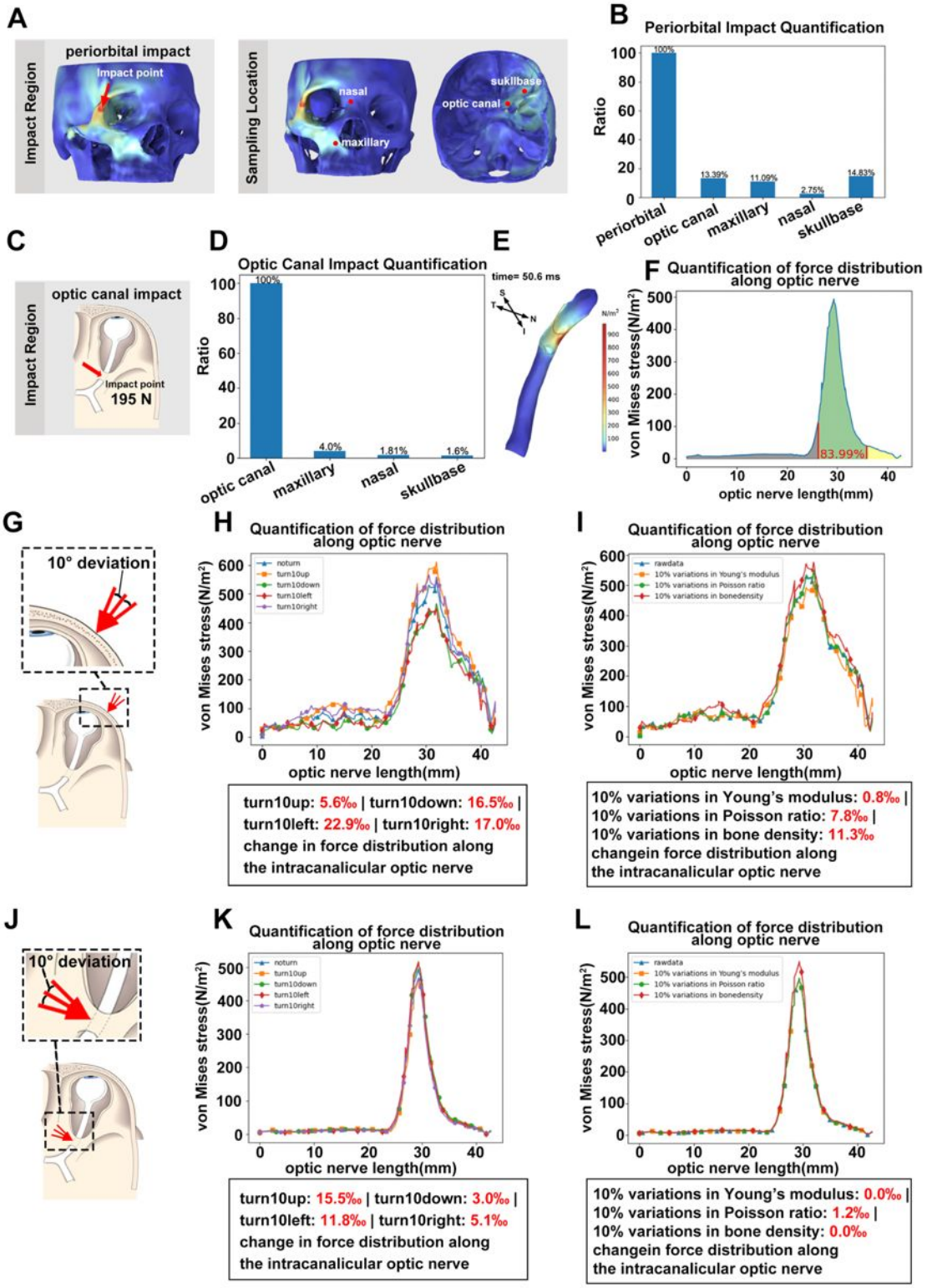

Figure 3 Computer simulation demonstrates that the optic nerve within the optic canal experiences the greatest mechanical stress after a clinically-relevant periorbital blunt impact.

(A) Representative simulations illustrating the site of periorbital impact and the locations for force distribution analysis.

(B) Quantification of force distribution at different analysis sites following periorbital impact at 50.6 ms.

(C) Schematic showing direct impact to the optic canal.

(D) Quantification of force distribution across different analysis sites following direct optic canal impact at 50.6 ms.

(E-F) Color-coded illustration and quantification of force distribution along the optic nerve following direct optic canal impact at 50.6 ms.

(G, J) Schematics illustrating deviation in impact angle by 10 degrees, both upward and downward, for periorbital (G) and optic canal (J) impacts.

(H-I, K-L) Quantification of force distribution fluctuation along the intracanalicular optic nerve by 10-degree deviations in impact direction and a 10% variation in bone mechanical properties (density, Young's modulus, Poisson's ratio) for periorbital impact (H, I) and optic canal impact (K, L).

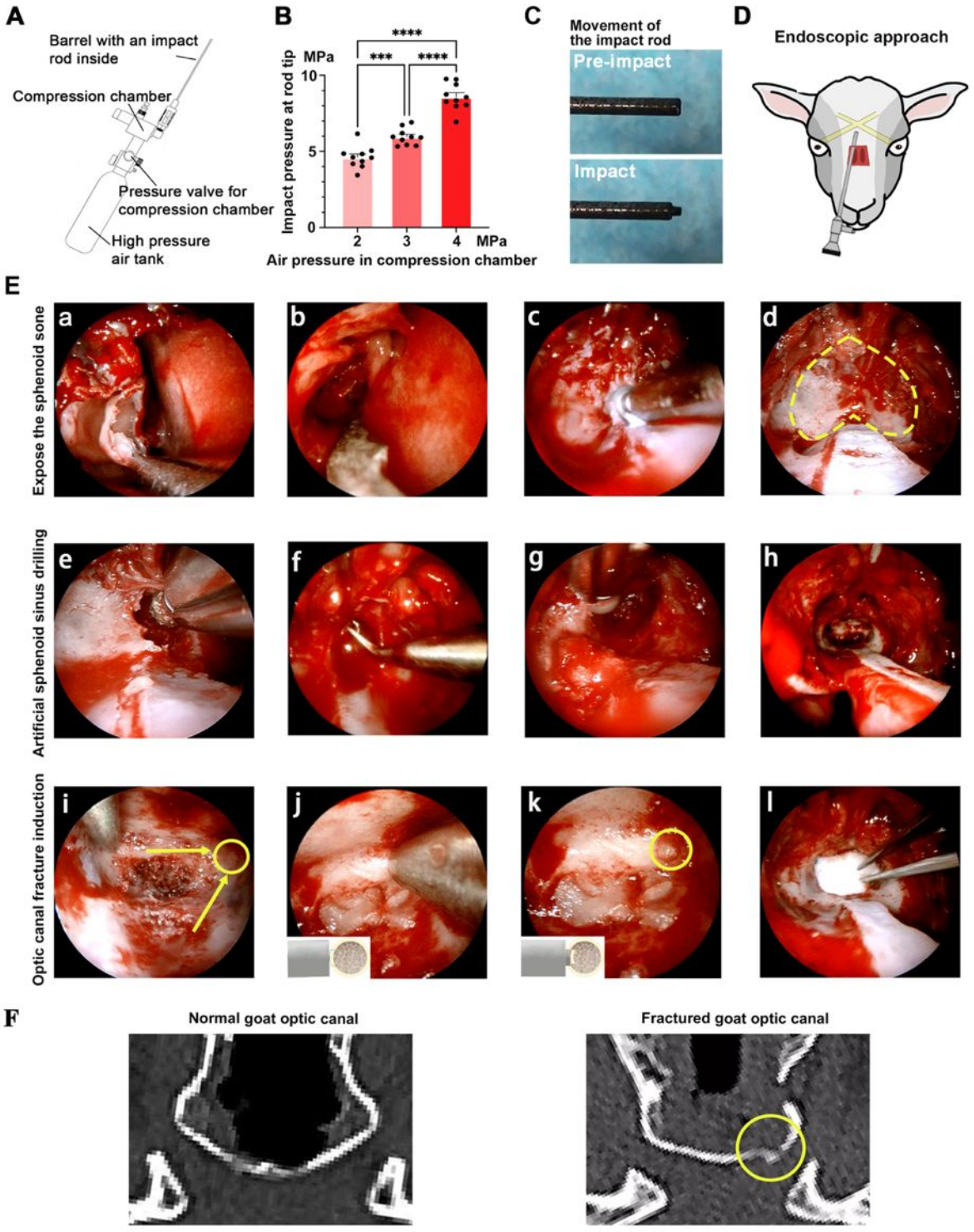

1003

1004 **Figure 4 Establishment of a reproducible TON goat model induced by optic canal**

1005 **fracture under transnasal endoscopy.**

(A) Schematic diagram of the gas-driven impactor, consisting of a high-pressure air tank, a compression chamber with a pressure valve, and a barrel containing the impact rod.

(B) Calibration of the device showing impact force at the rod tip under different air pressures in the compression chamber (2, 3, and 4 MPa). Each dot represents one impact (n = 10 per pressure level); data are shown as mean ± SD.

(C) Schematic diagram of the impact rod.

(D) Schematic diagram of the endoscopic approach.

(E) Intraoperative endoscopic views of key surgical steps. (a–d) Exposure of the anterior wall of the sphenoid bone after removal of the nasal septum, turbinates, and olfactory mucosa. The dotted yellow line in (d) outlines the bony window. (e–h) Drilling of the sphenoid body to create an artificial sphenoid sinus, providing direct access to the pre-chiasmatic optic canal. (i–l) Optic canal fracture induction: the impactor tip is seated against the anterior wall of the optic canal and a single impact generates a circumscribed bony fragment (yellow circle) that is displaced into the canal lumen.

(F) Representative CT images showing a normal goat optic canal (left), a post-impact goat optic canal with a depressed fracture fragment (right, yellow circle).

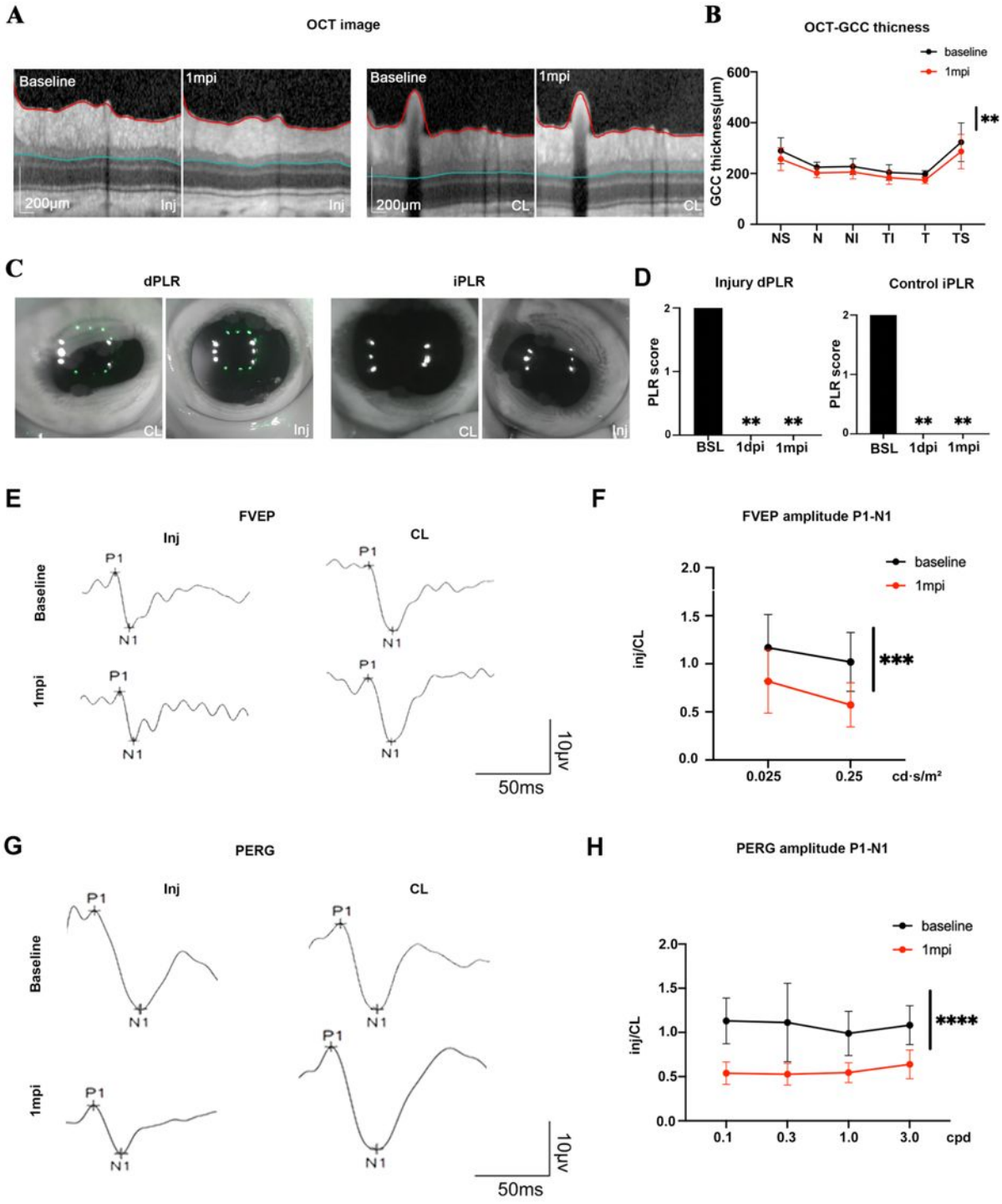

Figure 5 Structural and functional damage in a gas-driven goat model of TON.

(A) Representative peripapillary OCT scans of the injured eye at baseline and 1 month post-injury (1 mpi), with the GCC segmentation overlaid. Scale bar = 200 μm

(B) Quantification of GCC thickness in different macular sectors at baseline and 1 mpi (n = 8 goats; mean ± SD). In the injured eyes, GCC thickness exhibited significant thinning across all sectors. For example, in the temporal-superior (TS) sector, thickness decreased from 323.4 ± 76.1 μm at baseline to 286.5 ± 67.8 μm at 1 mpi (~11.4% reduction; P = 0.0018, two-way ANOVA, time factor).

(C) Representative infrared images of the direct (dPLR) and indirect (iPLR) pupillary light reflexes in the injured and contralateral eyes at 1 month post-injury (1 mpi).

(D) Quantification of PLR scores for the injured eye dPLR (left graph) and contralateral eye iPLR (right graph) at baseline (BSL), 1 day post-injury (1 dpi), and 1 month post-injury (1 mpi). Data are shown as mean ± SD; ns, not significant.

(E) Representative flash visual evoked potentials (FVEP) recorded from injured and contralateral eyes at baseline and 1 mpi.

(F) Ratios of FVEP P1–N1 amplitudes between injured and contralateral eyes (Inj/CL) at baseline and 1 mpi (n = 8; mean ± SD). The FVEP amplitude ratio exhibited a significant decline. At a flash intensity of 0.25 cd·s/m², the ratio decreased from 1.020 ± 0.306 at baseline to 0.573 ± 0.229 at 1 mpi (~43.8% reduction; P = 0.0010).

(G) Representative pattern electroretinogram (PERG) traces from injured and contralateral eyes at baseline and 1 mpi.

(H) Ratios of PERG P1–N1 amplitudes between injured and contralateral eyes (Inj/CL) at different spatial frequencies at baseline and 1 mpi (n = 8; mean ± SD). The PERG amplitude ratio demonstrated significant declines across all tested spatial frequencies. At 0.3 cpd, this ratio declined from 1.113 ± 0.444 at baseline to 0.528 ± 0.124 at 1 mpi (~52.6% reduction; P < 0.0001).

OCT-based GCC thickness in (B) was analyzed using two-way ANOVA with retinal sector and time (baseline vs 1 mpi) as factors. PLR data in (D) were analyzed using one-way ANOVA.

FVEP amplitude ratios in (F) were analyzed using two-way ANOVA with stimulus frequency and time as factors. PERG amplitude ratios in (H) were analyzed using the Scheirer–Ray–Hare non-parametric two-factor test with spatial frequency and time as factors. *P < 0.05, **P < 0.01, ***P < 0.001, ****P < 0.0001.

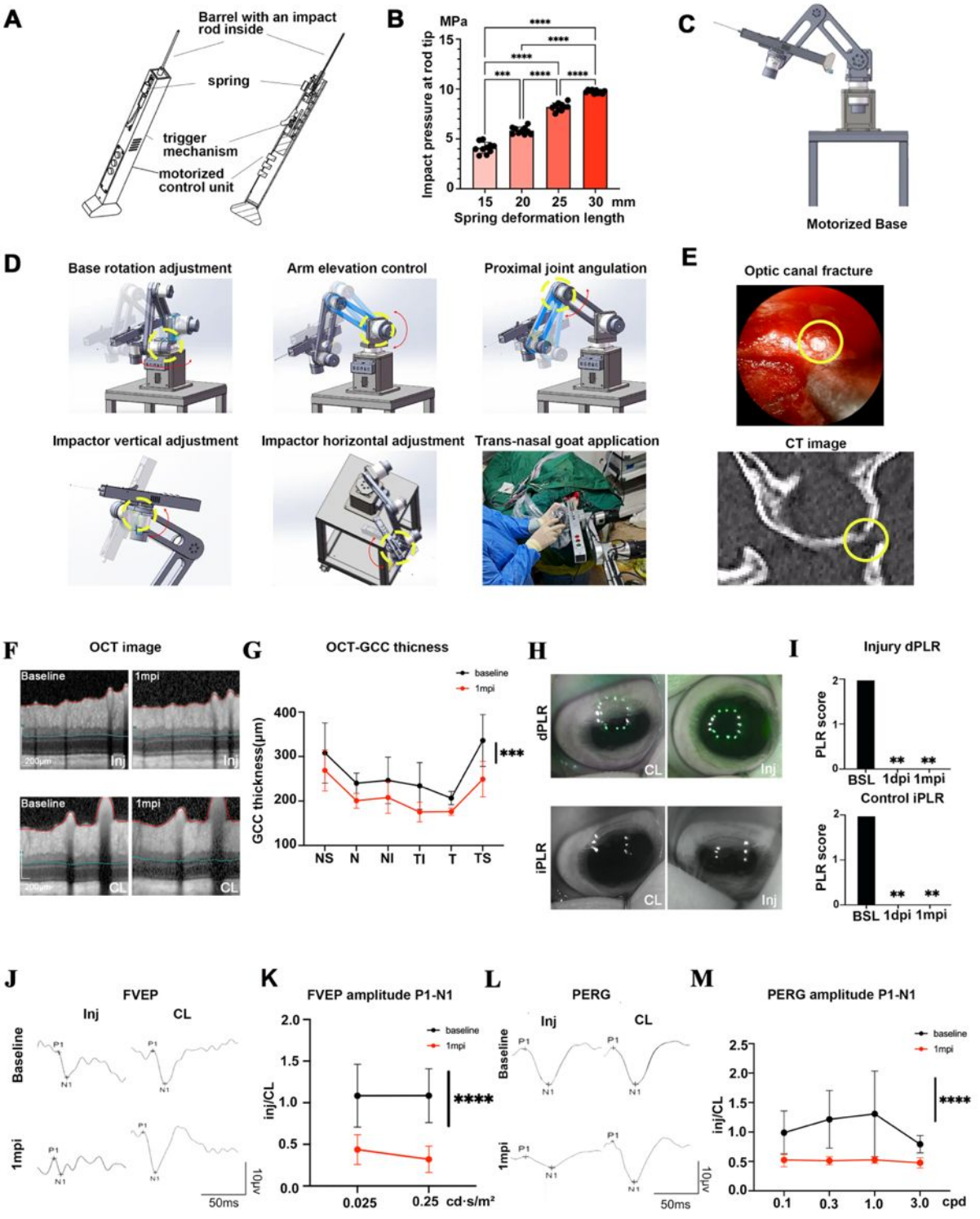

Figure 6 The elastic-energy driven goat model of traumatic optic neuropathy.

(A) Schematic diagram of the elastic-energy driven impact device used for optic canal fracture induction.

(B) Histogram summarizing the relationship between spring extension distance and impact force at the rod tip. Each bar represents one extension distance (n = 10 impacts per distance).

(C) Schematic of the motorized base with five independently driven joints, providing multi-axis positioning and recoil compensation during impact.

(D) Multi-axis stabilizing base for precise positioning of the impactor. Schematic views illustrate base rotation, arm elevation, proximal joint angulation, and vertical and horizontal adjustment of the impact head, which together allow flexible alignment of the impact rod with the optic canal. The right-bottom panel shows intraoperative transnasal application of the impact system in a goat.

(E) Verification of impacted optic canal fracture. Representative intraoperative endoscopic view (top) showing a circular bony fragment (yellow circle) that has been driven into and embedded within the optic canal, forming an impacted fracture. Postoperative CT image (bottom) confirms the impacted optic canal fracture, with the bony fragment lodged in the canal lumen (yellow circle) and exerting focal compression on the optic nerve.

(F) Representative OCT images of the ganglion cell complex (GCC) in the injured (Inj) and contralateral (CL) eyes at baseline and 1 month post-injury (1 mpi). Scale bar = 200 μm.

(G) Quantification of peripapillary GCC thickness in six sectors (NS, N, NI, TI, T, TS) at baseline and 1 mpi (n = 6 goats; mean ± SD). In the injured eyes, GCC thickness exhibited significant thinning across all sectors. For example, in the temporal-superior (TS) sector, thickness decreased from 336.2 ± 58.2 μm at baseline to 249.2 ± 39.8 μm at 1 mpi (~25.9% reduction; P = 0.00022).

(H) Representative infrared PLR images showing loss of the direct PLR (dPLR) in the injured eye and preserved indirect PLR (iPLR) in the contralateral eye at 1 dpi, consistent with a relative afferent pupillary defect.

(I) Quantification of dPLR scores in the injured eye and iPLR scores in the contralateral eye at baseline (BSL), 1 day (1 dpi), and 1 month (1 mpi) post-injury.

(J) Representative FVEP waveforms recorded from injured and contralateral eyes at baseline and 1 mpi (flash intensities 0.025 and 0.25 cd·s/m²).

(K) Relative FVEP P1–N1 amplitude ratios (Inj/CL) at the two flash intensities (n = 6; mean ± SD). The FVEP amplitude ratio exhibited a significant decline. At a flash intensity of 0.25 cd·s/m², the ratio decreased from 1.086 ± 0.323 at baseline to 0.321 ± 0.158 at 1 mpi (~70.4% reduction; $P < 0.0001$).

(L) Representative PERG waveforms from injured and contralateral eyes at baseline and 1 mpi (spatial frequency 0.3 cpd).

(M) Relative PERG P1–N1 amplitude ratios (Inj/CL) across spatial frequencies (0.1–3.0 cpd; n = 6; mean ± SD). The PERG amplitude ratio demonstrated significant declines across all tested spatial frequencies. At 0.3 cpd, this ratio declined from 1.215 ± 0.489 at baseline to 0.513 ± 0.068 at 1 mpi (~57.8% reduction; $P < 0.0001$).

Impact-force data in (B) were analyzed using ordinary one-way ANOVA with Tukey's multiple comparisons test. OCT-based GCC thickness in (G) was analyzed using the Scheirer–Ray–Hare non-parametric two-factor test with retinal sector and time (baseline vs 1 mpi) as factors. PLR data in (I) were analyzed using one-way ANOVA. FVEP amplitude ratios in (K) were analyzed using two-way ANOVA with stimulus intensity and time as factors. PERG amplitude ratios in (M) were analyzed using the Scheirer–Ray–Hare non-parametric two-factor test with spatial frequency and time as factors. Data are mean ± SD; *$P < 0.05$, $P < 0.01$, *$P < 0.001$, ****$P < 0.0001$.

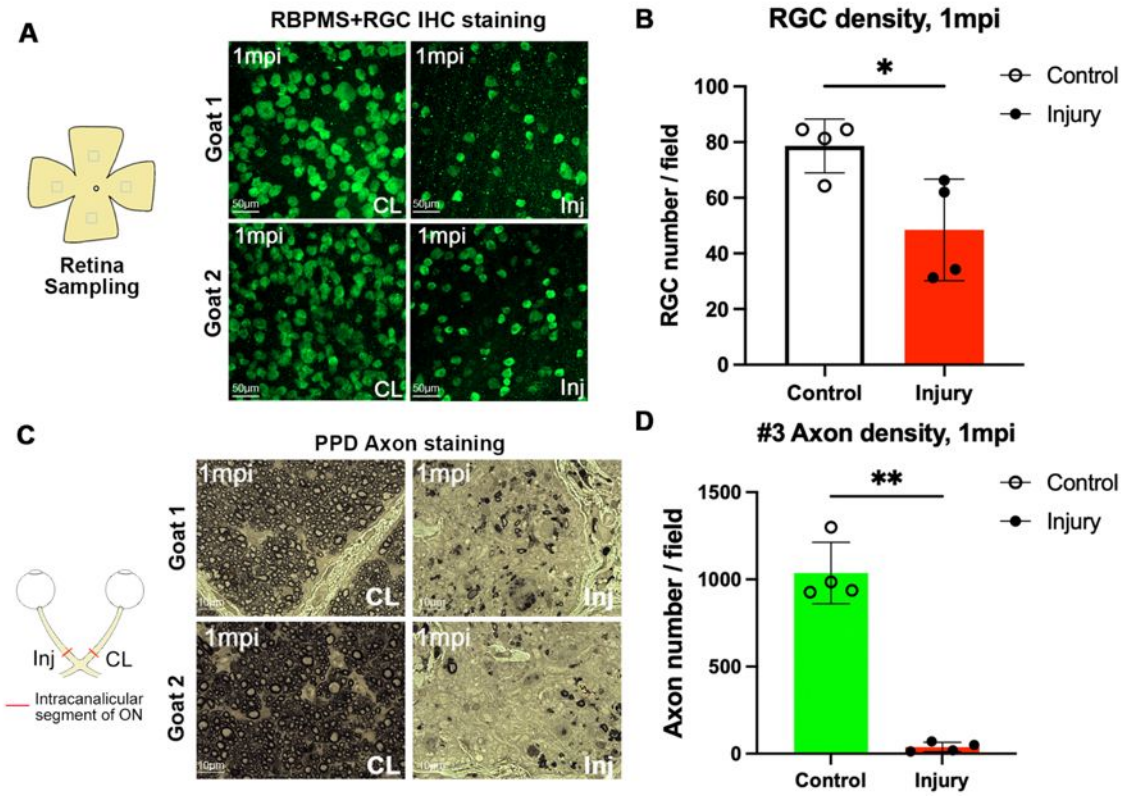

Figure 7. Histological and quantitative evaluation of retinal ganglion cell (RGC) survival and optic nerve axonal degeneration in the caprine TON model at 1 month post-injury (1mpi).

(A) Representative RBPMS immunofluorescence staining of retinal flat mounts from the uninjured contralateral (CL) and injured (Inj) eyes. Scale bar = 50 μm.

(B) Quantification of RGC survival (count per field). The injured eyes exhibited a significant reduction in RGC compared to the uninjured controls. Data are presented as mean ± SD (n = 4 per group). *P < 0.05 by paired Student's t-test.

(C) Representative paraphenylenediamine (PPD) staining of optic nerve cross-sections at the intracanalicular segment. The control nerves display densely packed, intact myelin sheaths, whereas the injured nerves exhibit severe axonal loss, myelin sheath disruption, and extensive vacuolization. Scale bar = 10 μm.

(D) Quantification of viable axons (count per field) in the intracanalicular segment, confirming massive axonal depletion following impact. Data are presented as mean ± SD (n = 4 per group). **P < 0.01 by paired Student's t-test.

1133 **Table S1. Materials and supplies.**

Materials	Company	Catalogue no.
Saanen goat	Caimu Livestock Company, China	-
Propofol	Fresenius Kabi, Sweden	-
Isoflurane	RWD Life Science, China	-
Xylazine	Jilin Huamu Animal Health Products Co. LTD, China	-
periosteal elevator	JZ Classic, China	-
Nasal Mucosa Knives	JZ Classic, China	H7Z150
Sinuscopes	HENKE SASS WOLF, Germany	7197200300
Endoscopic microdebrider	Medtronic, America	1884004
Endoscopic microdrill	Medtronic, America	1882969
Closed IV catheter system	BD Shanghai Medical Device Co., Ltd, China	383019
Hemocoagulase Atrox	Penglainuokang Pharmaceutical, China	-
Heidelberg Spectralis OCT system	Heidelberg Engineering (Germany)	
Visual Electrophysiology System	Visual Electrophysiology System	GT-2008V-III
GraphPad Prism	GraphPad Prism	RRID:SCR_002798

1134
1135

Table S2 Perioperative Morbidity, Mortality, and Exclusion Rates by Impactor Type

Impactor	Total Animals (N)	PLR grade ≥2	PLR grade <2	Exclusion Rate	Perioperative Morbidity/Mortality
Gas driven	20	18	2	10.00%	2/0
Elastic-energy driven	18	18	0	0.00%	1/0

Note: Perioperative morbidity refers strictly to mild, transient rhinorrhea observed in 3 animals post-surgery, which fully resolved after a 5-day course of antibiotic treatment. Exclusions were solely due to failure to meet the acute functional deficit criterion (PLR grade difference < 2) within 24 hours post-impact. No animals were excluded due to surgical complications.

Table S3 Statistic Power Analysis

Figure location	Statistical method	One/two-tailed	Residuals passed normality test?	Residuals passed homogeneity of variance test?	N values	P values (List post-hoc test pvalue, if it exits)	F values / t values / other statistic values (Primary test)	Degrees of freedom (Primary test)	Power, 1-β	Sample Size Calculation	Note
Fig. 5B	Two-way ANOVA with Sidak's multiple comparisons test	two-tailed	Yes	Yes	n=8	Main effect of Time: P=0.0018	F = 10.34	DFn=1, DFd=84	84.30%	n=12	
Fig. 5F	Two-way ANOVA with Sidak's multiple comparisons test	two-tailed	Yes	Yes	n=8	Main effect of Time: P=0.0010	F = 13.6	DFn=1, DFd=28	86.74%	n=7	
Fig. 5H	Scheirer–Ray–Hare non-parametric two-factor test	two-tailed	No	/	n=8	Main effect of Time: P<0.0001	H = 31.92	DF=1	91.53%	n=7	
Fig. 6G	Scheirer–Ray–Hare non-parametric two-factor test	two-tailed	No	/	n=6	Main effect of Time: P=0.00022	H = 13.61	DF=1	85.20%	n=4	
Fig. 6K	Two-way ANOVA with Sidak's multiple comparisons test	two-tailed	Yes	Yes	n=6	Main effect of Time: P<0.0001	F = 39.4	DFn=1, DFd=20	99.66%	n=4	
Fig. 6M	Scheirer–Ray–Hare non-parametric two-factor test	two-tailed	No	/	n=6	Main effect of Time: P<0.0001	H = 31.92	DF=1	87.98%	n=5	
Fig. 7B	Paired t-test	two-tailed	Yes	/	n=4	Control vs. Injury: P=0.0340	t = 3.711	DF=3	68.46%	n=5	
Fig. 7D	Paired t-test	two-tailed	Yes	/	n=4	Control vs. Injury: P<0.0001	t = 11.23	DF=3	100.00%	n=2	

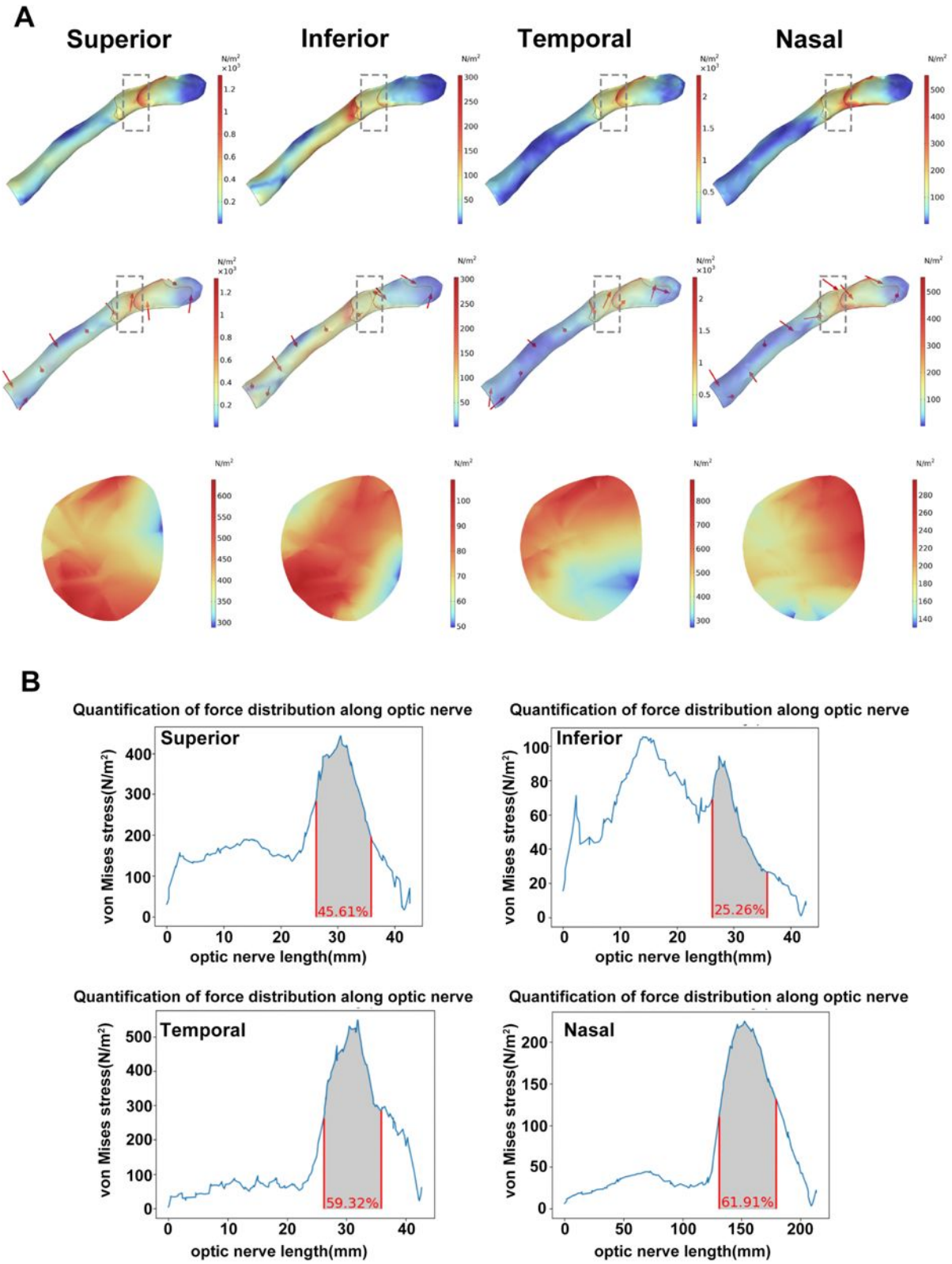

Figure S1. Comparative analysis of force distribution in the optic nerve following periorbital impacts at different locations

(A) Illustrations of force distribution along the optic nerve (upper panel), directions of force along the optic nerve (middle panel), and force distribution through the cross-section of the mid intracanalicular optic nerve (lower panel) at 50.6 ms, when the periorbital impact reached its maximum strength following periorbital impacts at various locations (Superior, Inferior, Temporal, Nasal). The grey dashed box indicates the intracanalicular segment of the optic nerve, while the red arrow displays the direction of the impact force applied to the nerve. **(B)** Schematic depicting the locations of periorbital impacts and quantification of force distribution along the optic nerve at 50.6 ms following periorbital impacts at various locations.

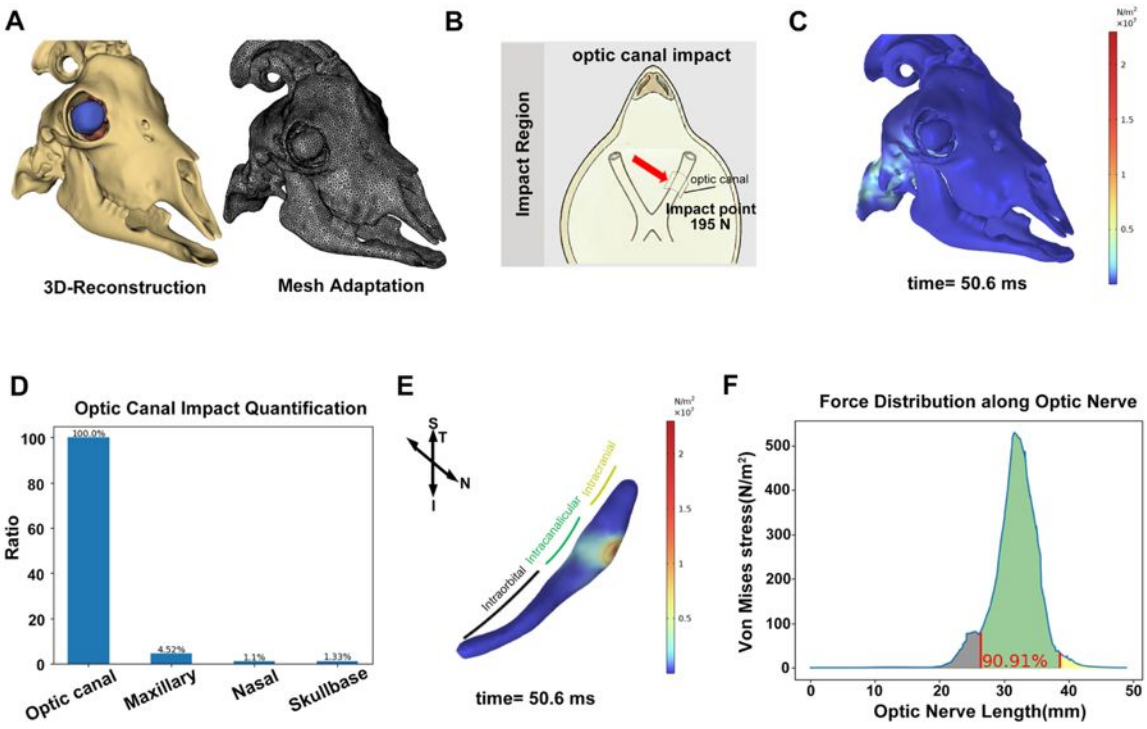

1157
1158 **Figure S2 Goat-specific finite element analysis demonstrating highly localized stress**
1159 **concentration and biomechanical equivalence following direct optic canal impact.**

1160 (A) Representative images demonstrating the development of the caprine-specific
1161 biomechanical model, including 3D-reconstruction and mesh adaptation based on high-
1162 resolution micro-CT scans of a Saanen goat skull.

1163 (B) Schematic showing direct impact to the goat optic canal.

1164 (C) Color-coded displays showing global force propagation across the caprine skull at the
1165 moment of peak direct impact to the right optic canal (at 50.6 ms).

1166 (D) Quantification of force distribution across different analysis sites following direct optic
1167 canal impact at 50.6 ms.

1168 (E, F) Color-coded illustration and quantification of force distribution along the ON at 50.6
1169 ms.

1170

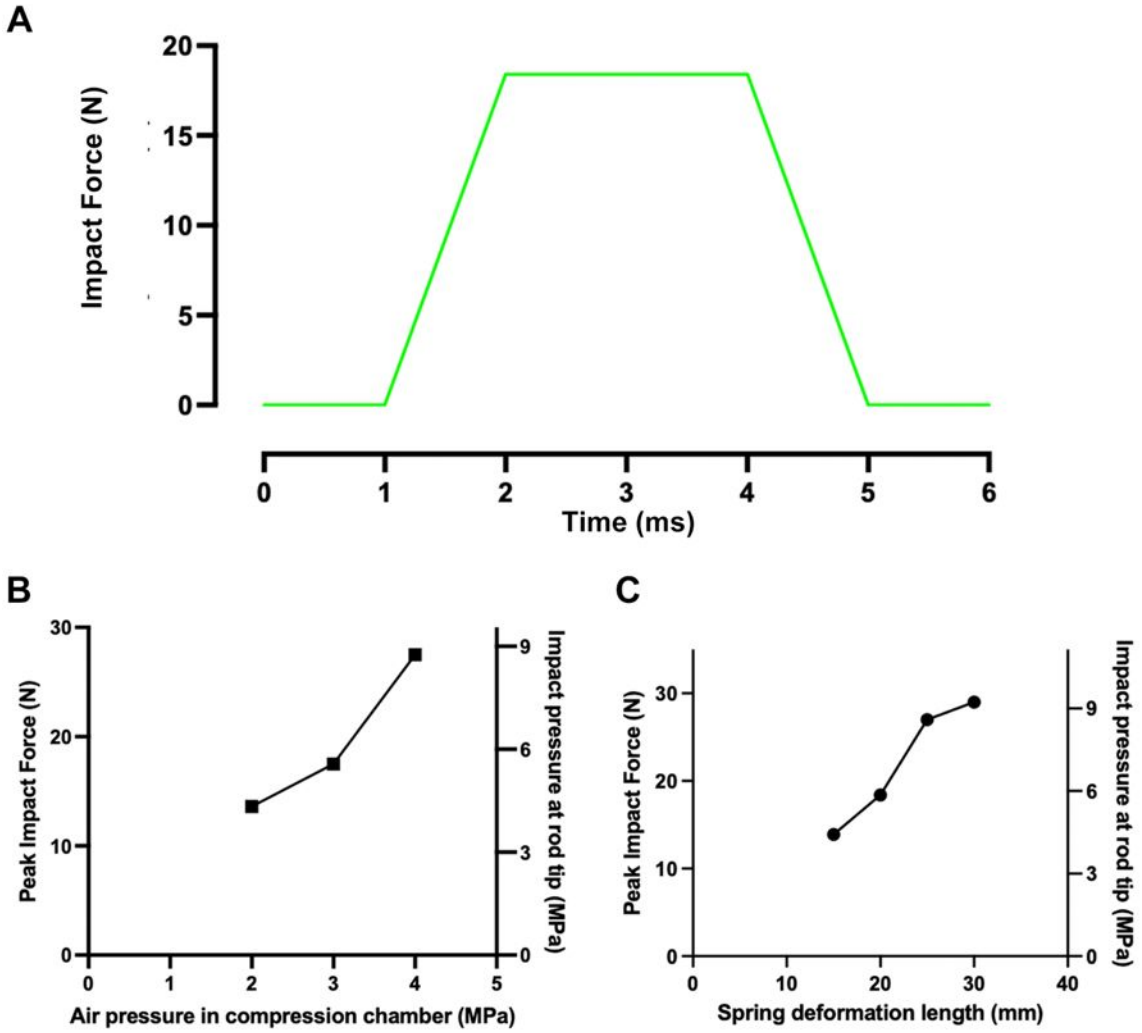

D

Impactor Parameter	Specification
Rod Tip Diameter	2.0 mm
Rod Tip Stroke Length	2.0 mm
Dwell Time	4.0 ms
Peak Impact Velocity	2.0 m/s

Figure S3. Quantitative engineering specifications and dynamic kinetic characterization of the TON impactor systems.

(A) Representative dynamic force-time impulse waveform captured via a high-frequency load cell for the elastic-energy impactor at the standardized 20 mm spring deformation setting. The clean, trapezoidal impulse curve confirms a deterministic, single dynamic energy transfer event with a peak force of 18.7 N and a sharply controlled dwell time of 4.0 ms, completely devoid of unpredictable secondary reverberations or "double-hits."

(B) Dual-axis force calibration curve of the first-generation gas-driven impactor. The left Y-axis indicates peak impact force (N), while the derived secondary Y-axis (right) details the localized dynamic impact stress (MPa). Testing across escalating air pressure settings (2 to 4 MPa) yielded a predictable mechanical output, with the standardized 3 MPa in vivo modeling setting generating a peak impact force of 17.5 N (corresponding to 5.57 MPa of dynamic stress).

(C) Complementary dual-axis force calibration curve of the optimized second-generation elastic-energy impactor across sequential spring deformation lengths. Notably, the standardized in vivo setting (20 mm, yielding 18.7 N) achieves high biomechanical comparability with the standardized setting of the early gas-driven prototype (3 MPa, yielding 17.5 N), ensuring translational mechanical continuity between device iterations.

(D) Standardized technical specifications of the elastic-energy impactor used for the 20 mm spring deformation setting.

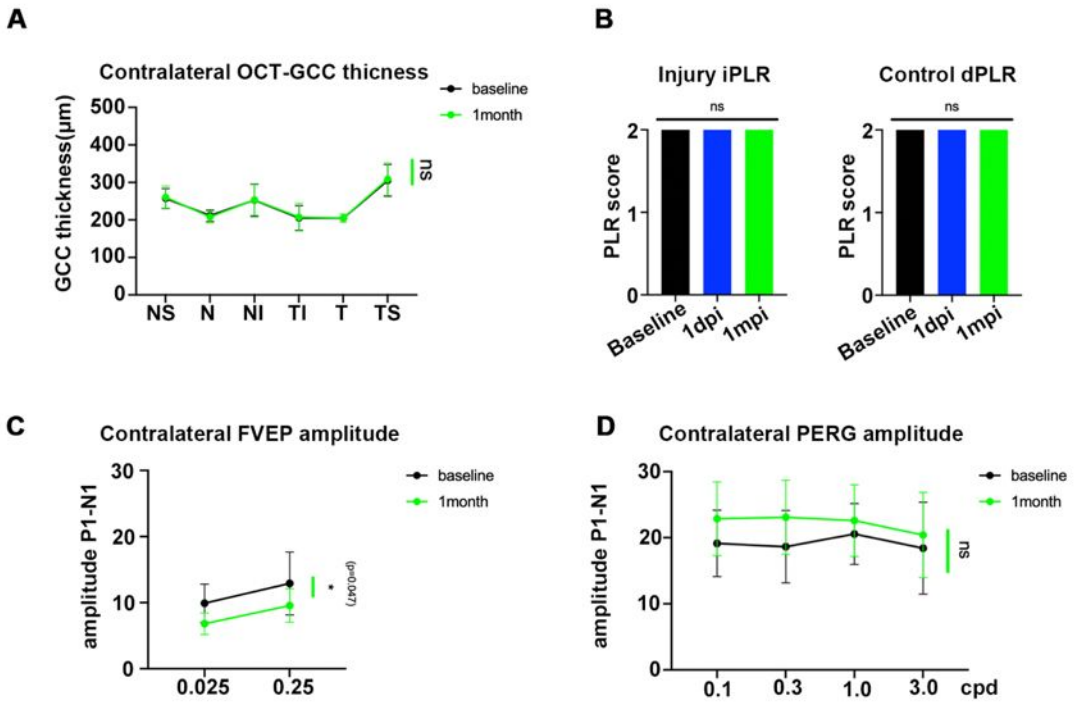

1195

1196 **Figure S4 Visual function and GCC thickness are preserved in the contralateral eyes**

1197 **after TON induction with a gas-driven device.**

1198 **(A–D)** Gas-driven impact device cohort (n = 8 goats).

1199 **(A)** OCT-derived GCC thickness in different macular sectors of the contralateral eyes at

1200 baseline and 1 mpi (NS, nasal-superior; NI, nasal-inferior; TI, temporal-inferior; T, temporal;

1201 TS, temporal-superior).**(B)** PLR scores in the TON cohort showing preserved indirect PLR

1202 (iPLR) in the injured eyes and direct PLR (dPLR) in the contralateral eyes at baseline, 1 day

1203 post-injury (1 dpi) and 1 mpi (0–2 grading scale; ns). **(C)** FVEP P1–N1 amplitudes of the

1204 contralateral eyes at two flash intensities (0.025 and 0.25 cd·s/m²) at baseline and 1 mpi. **(D)**

1205 PERG P1–N1 amplitudes recorded from the contralateral eyes at different spatial frequencies

1206 (0.1, 0.3, 1.0, and 3.0 cpd) at baseline and 1 mpi.

1207 Data are presented as mean ± SD. OCT, PLR, FVEP and PERG data in (A–D) were analyzed

1208 using two-way ANOVA with appropriate post hoc multiple comparisons. ns, not significant.

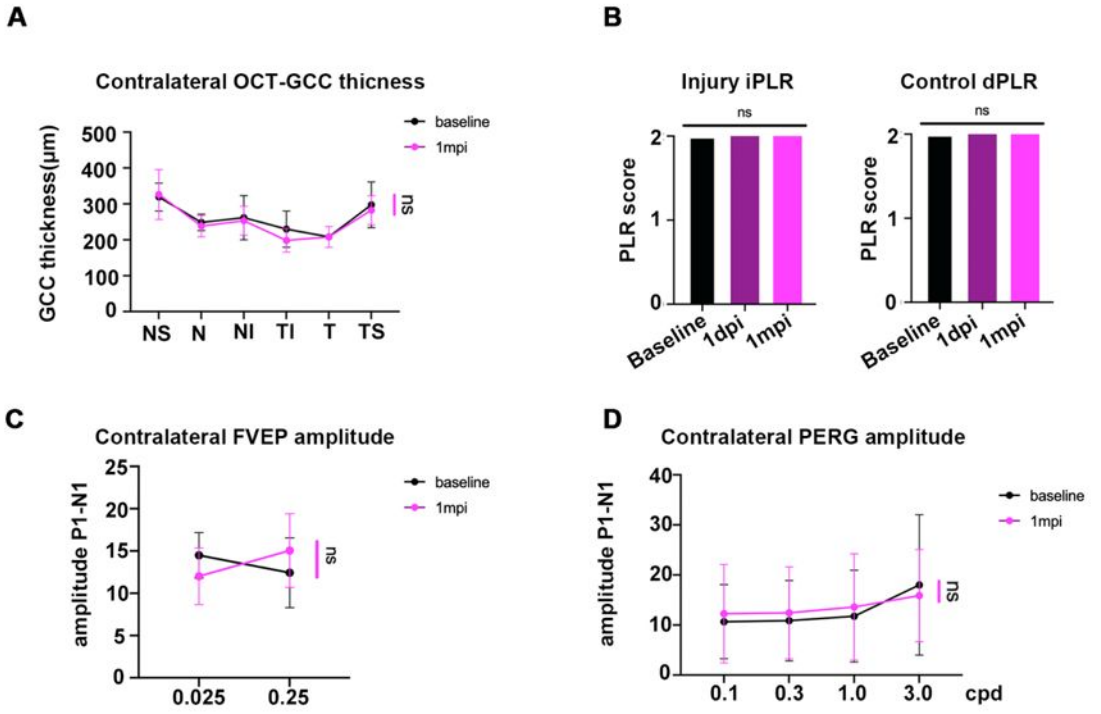

Figure S5 Visual function and GCC thickness are preserved in the contralateral eyes after TON induction with an elastic-energy driven device.

(A–D) Elastic-energy driven impact device cohort (n = 6 goats).

(A) OCT-derived GCC thickness in the contralateral eyes at baseline and 1 mpi, **(B)** PLR scores in the TON cohort showing preserved indirect PLR (iPLR) in the injured eyes and direct PLR (dPLR) in the contralateral eyes at baseline, 1 day post-injury (1 dpi) and 1 mpi (0–2 grading scale; ns). **(C)** FVEP P1–N1 amplitudes, and **(D)** PERG P1–N1 amplitudes.

Data are presented as mean ± SD. OCT, PLR, FVEP and PERG data in (A–D) were analyzed using two-way ANOVA with appropriate post hoc multiple comparisons. ns, not significant.

标题：经鼻内镜构建伴视神经管骨折的仿生山羊外伤性视神经病变模型

短标题：外伤性视神经病变大动物模型

余钟豪[1,2#]; 段恒卓[4#]; 杨桐赫[1,2#]; 曹毅[1,2]; 田树东[1,2]; 吴欢[1,2]; 张家乐[1,2]; 汪玥[1,2]; 周芮欣[1,2]; 卢圣建[1,2]; 许博悦[1,2]; 李梦云[6]; 夏添[1,5]; 张思[7]; 陈浩迪[1,2]; 黄书睿[1,2]; 张逸夔[1,2*]; 杨健[4,1*]; 吴文灿[1,2,3*]

[1] 国家重点实验室，眼视光医院, 温州医科大学, 温州, 中国

[2] 浙江省视觉通路重建重点实验室, 眼视光医院, 温州医科大学, 温州, 中国

[3] 瓯江实验室（浙江省再生医学，视觉与脑健康实验室）, 温州, 浙江, 中国

[4] 北京市混合现实与新型显示工程技术研究中心, 光电学院, 北京理工大学; 北京, 100081, 中国

[5] 金华市中心医院眼科， 浙江大学附属金华医院; 金华, 浙江, 321000, 中国

[6] 医学研究中心, 绍兴市人民医院, 浙江大学绍兴医院; 绍兴, 浙江, 312035, 中国

[7] 佛山市人民医院眼科; 佛山, 广东, 528000, 中国.

余钟豪,段恒卓, 杨桐赫同等贡献于这项工作。

* 收信人地址。

张逸夔: zhang.yikui@wmu.edu.cn

杨健: jyang@bit.edu.cn

吴文灿: wuwencan@wmu.edu.cn

摘要

外伤性视神经病变（TON）是颅脑钝性创伤后不可逆视力损伤的主要病因。目前缺乏能够真实模拟人类外伤性视神经病变、且贴合临床特征的大动物模型，极大阻碍了相关转化医学研究的开展。现有的啮齿类动物模型无法复刻视神经管骨折这一众多外伤性视神经病变患者的核心损伤机制。

本研究联合高精度有限元分析与迭代工程设计，构建了可稳定重复的山羊外伤性视神经病变模型。首先建立高分辨率人体头部有限元模型，分析外力向视神经的传导规律。在临床常见的眶周外力冲击条件下，应力优先集中于视神经管内段，于冲击后 50.6 毫秒达到约 500 N/m² 的峰值力密度，较眶内段视神经高出约 5 倍。仿真结果进一步显示：直接冲击视神经管可在大幅降低外力输入的前提下，产生与眶周冲击相近的管内段应力 —— 直接冲击仅需 195 N，而眶周冲击则需 3900 N。

基于上述仿真结论，本研究研发出经鼻内镜冲击装置，可稳定造成山羊视神经管骨折。造模后 24 小时内，通过特征性相对性传入性瞳孔障碍（RAPD） 确诊外伤性视神经病变；伤后 1 个月，14 只实验山羊的神经节细胞复合体（GCC）厚度下降 10%~20%，闪光视觉诱发电位（FVEP）及图形视网膜电图（PERG）振幅比值下降 40%~65%（所有指标 $P \leq 0.001$），且对侧健眼结构与功能均保持正常。

本研究建立了一种稳定可靠、标准化、高度贴合临床的大动物实验平台，可为外伤性视神经病变的病理机制研究提供支撑。

关键词：

外伤性视神经病变；有限元分析；大动物模型；经鼻内窥镜；视神经管